

GPCR activation and GRK2 assembly by a biased intracellular agonist

<https://doi.org/10.1038/s41586-023-06395-9>

Received: 10 October 2022

Accepted: 3 July 2023

Published online: 2 August 2023

 Check for updates

Jia Duan^{1,2,3,8}, Heng Liu^{1,8}, Fenghui Zhao^{4,8}, Qingning Yuan¹, Yujie Ji^{1,3}, Xiaoqing Cai⁴, Xinheng He^{1,3}, Xinzhu Li¹, Junrui Li¹, Kai Wu¹, Tianyu Gao^{1,5}, Shengnan Zhu¹, Shi Lin⁶, Ming-Wei Wang⁶, Xi Cheng¹, Wanchao Yin^{1,2,3}, Yi Jiang⁷, Dehua Yang^{3,4,6} & H. Eric Xu^{1,3,5}

Phosphorylation of G-protein-coupled receptors (GPCRs) by GPCR kinases (GRKs) desensitizes G-protein signalling and promotes arrestin signalling, which is also modulated by biased ligands^{1–6}. The molecular assembly of GRKs on GPCRs and the basis of GRK-mediated biased signalling remain largely unknown owing to the weak GPCR–GRK interactions. Here we report the complex structure of neurotensin receptor 1 (NTSR1) bound to GRK2, $\text{G}\alpha_q$ and the arrestin-biased ligand SBI-553⁷. The density map reveals the arrangement of the intact GRK2 with the receptor, with the N-terminal helix of GRK2 docking into the open cytoplasmic pocket formed by the outward movement of the receptor transmembrane helix 6, analogous to the binding of the G protein to the receptor. SBI-553 binds at the interface between GRK2 and NTSR1 to enhance GRK2 binding. The binding mode of SBI-553 is compatible with arrestin binding but clashes with the binding of $\text{G}\alpha_q$ protein, thus providing a mechanism for its arrestin-biased signalling capability. In sum, our structure provides a rational model for understanding the details of GPCR–GRK interactions and GRK2-mediated biased signalling.

GPCRs comprise the largest family of cell surface receptors. GPCR signalling is primarily mediated by two types of downstream effectors: G proteins and arrestins. The switch of GPCR signalling from G-protein pathways to arrestin pathways is controlled by a small family of GPCR kinases, GRKs, which phosphorylate either the receptor C-terminal tail or the third intracellular loop^{1–3} (ICL3). Phosphorylation of GPCRs promotes recruitment of arrestin, which blocks G-protein binding and desensitizes G-protein signalling³. Because drugs that selectively activate either G-protein pathways or arrestin pathways (biased signalling) are proposed to have good therapeutic and safety indices^{4,5}, the mechanism of GPCR biased signalling has been a subject of intensive research over the past two decades.

GRK2, along with GRK1, are the prototypes of GRKs that belong to the AGC family of serine/threonine kinases^{8–10}. There are seven GRKs, which can be grouped into the rhodopsin kinase subfamily (GRK1 and GRK7), the β -adrenergic receptor kinase subfamily (GRK2 and GRK3) and the GRK4 subfamily⁹ (GRK4, GRK5 and GRK6). All GRKs share conserved sequence features and structural arrangements¹¹. At the N terminus is a conserved segment that forms a helix in the active GRK structures^{12,13}, followed by the first eight helices of a regulatory G-protein signalling homology domain^{10,14} (RHD). The kinase domain (KD) is inserted into a loop between helices 8 and 9 of the RHD, a conserved domain of a nine-helix bundle found in regulatory G-protein signalling proteins¹⁵. Following the kinase domain and helix 9 of the RHD are the less conserved C-terminal GRK domains, which are mainly responsible for membrane binding¹⁶. In the case of GRK2, the C terminus contains a

pleckstrin homology domain (PHD) that interacts with $\text{G}\beta\gamma$ subunits of G protein¹⁷. The RHD of GRK2 also interacts with $\text{G}\alpha_q$ when it is in complex with GTP¹⁸. The binding of both $\text{G}\alpha_q$ and $\text{G}\beta\gamma$ subunits to GRK2 facilitates its membrane association^{17,18}.

Similar to other GPCR signal transducers such as G proteins and arrestins, GRKs are rest in the basal state, and can be recruited and activated by active GPCRs³. The molecular basis for how GPCR signal transducers recognize and regulate GPCR signalling has been a focus of research in GPCR structural biology^{13,16,19–22}. Structures of many GPCR–G protein complexes and GPCR–arrestin complexes have been solved—they reveal that both G proteins and arrestins recognize the open cytoplasmic pocket induced by the outward movement of transmembrane helix 6 (TM) in the activated class A, B and F GPCRs^{20,21,23–26}. Owing to much weaker interactions between GPCRs and GRKs, obtaining a structure of a GPCR–GRK complex at high resolution is technically challenging. A structure of rhodopsin in complex with GRK1 has provided a breakthrough view of the overall assembly of GRK1 with rhodopsin via its N-terminal helix¹³. However, the relatively low resolution of the structure lacks density for the conserved RHD domain of GRK1 and limits detailed understanding of the interactions between rhodopsin and GRK1, and of GRK1 activation by the active rhodopsin.

NTSR1 is a class A GPCR that is regulated by an endogenous peptide ligand, neurotensin²⁷ (NTS). Upon activation, NTSR1 couples to various signal effectors, including several subtypes of G proteins (primarily G_q), GRKs and arrestins, to mediate neurotransmission and neuromodulation in the central nervous system^{27–29}. Because of its

¹State Key Laboratory of Drug Research, Shanghai Institute of Materia Medica, Chinese Academy of Sciences, Shanghai, China. ²Zhongshan Institute for Drug Discovery, Shanghai Institute of Materia Medica, Chinese Academy of Sciences, Zhongshan, China. ³University of Chinese Academy of Sciences, Beijing, China. ⁴The National Center for Drug Screening, Shanghai Institute of Materia Medica, Chinese Academy of Sciences, Shanghai, China. ⁵School of Life Science and Technology, ShanghaiTech University, Shanghai, China. ⁶Research Center for Deepsea Bioresources, Sanya, Hainan, China. ⁷Lingang Laboratory, Shanghai, China. ⁸These authors contributed equally: Jia Duan, Heng Liu, Fenghui Zhao. [✉]e-mail: duanjia@simm.ac.cn; dhyang@simm.ac.cn; eric.xu@simm.ac.cn

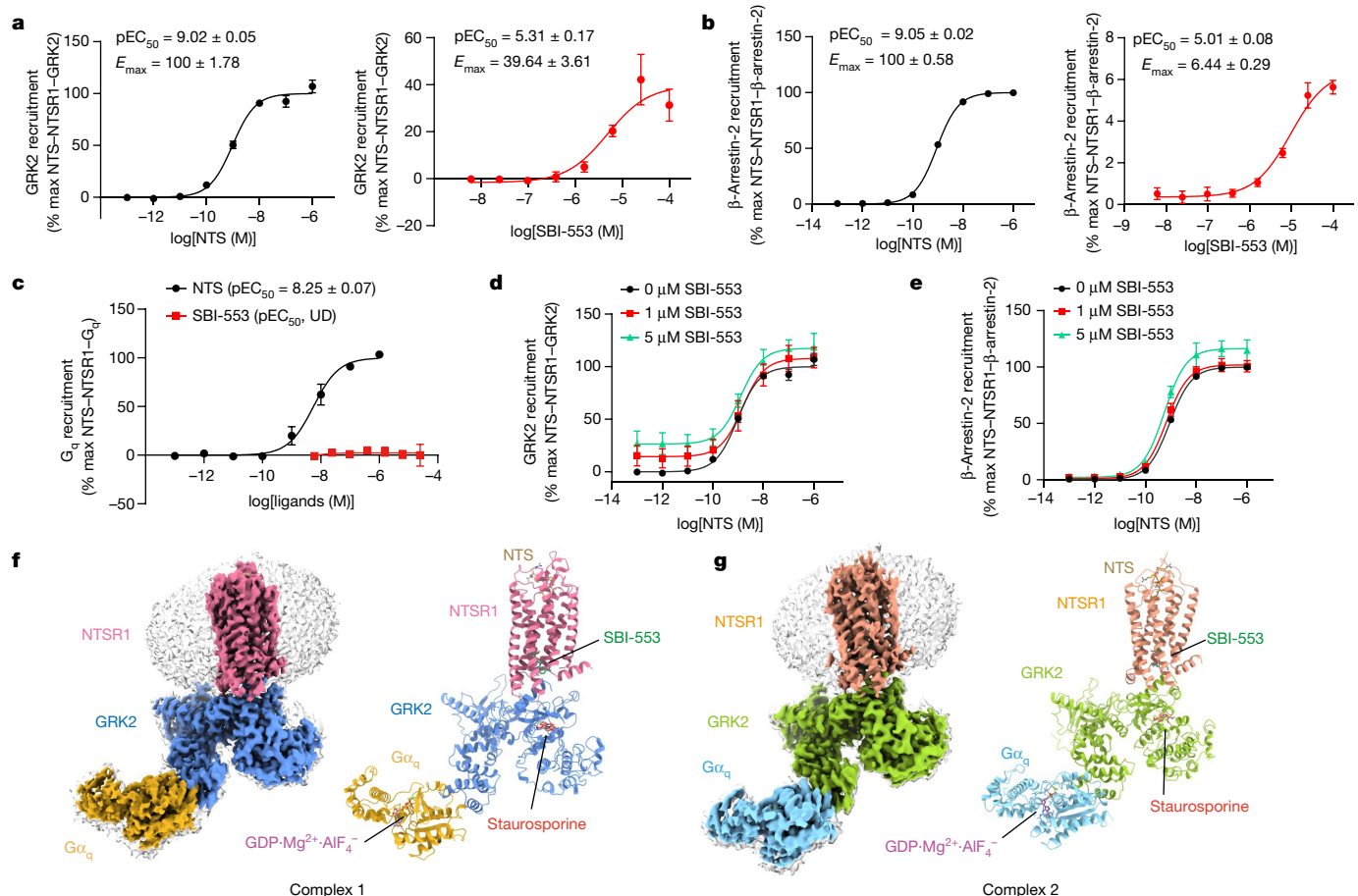


Fig. 1 | Cryo-EM structures of NTSR1-GRK2-G_q complexes. **a–c**, NanoBiT assay showing NTS and SBI-553 induced GRK2 (**a**), β-arrestin-2 (**b**) and G_q (**c**) recruitment to NTSR1. **d,e**, GRK2 (**d**) or β-arrestin-2 (**e**) recruitment to NTSR1 induced by co-treatment with NTS and vehicle or 1 or 5 μM SBI-553. Recruitment

is expressed as a percentage of the maximum (max) amount of the indicated protein complex. Data are mean ± s.d. from three independent experiments ($n=3$) performed in duplicate. **f,g**, Cryo-EM density maps and ribbon representation of NTSR1-GRK2-G_q complex 1 (**f**) and complex 2 (**g**).

diverse physiological roles, NTSR1 has been proposed as a drug target for addiction, obesity, analgesia, cancer, Parkinson's disease and schizophrenia⁷. Structures of NTSR1 in complex with G_i or β-arrestin have been determined by cryo-electron microscopy^{23,24,30} (cryo-EM). Notably, SBI-553, a β-arrestin-biased allosteric ligand of NTSR1 that antagonizes G_q signalling, selectively reduces addictive behaviours without the unwanted side effects of hypotension, hypothermia and motor impairment, which are typically associated with balanced agonism of NTSR1 induced by neurotensin⁷. However, the structural basis of β-arrestin-biased agonism of SBI-553 remains unknown. In this Article, we report the structure of NTSR1 bound to NTS, GRK2, G_q and SBI-553 at a global nominal resolution of 3.1 Å, which reveals detailed interactions between NTSR1 and GRK2 and provides a molecular explanation for the ability of SBI-553 to induce interactions between NTSR1 and GRK2.

Complex assembly and structure determination

To identify a stable GPCR-GRK2 complex, we used Tango assays³¹ to screen various members of class A GPCRs for their interactions with GRK2. Using these assays, we identified NTSR1 as one of the strongest receptors that interact with GRK2 in the presence of its endogenous peptide agonist NTS (Extended Data Fig. 1a). Both NTS and SBI-553 promoted the recruitment of GRK2 (Fig. 1a and Extended Data Table 2) and β-arrestin-2 (Fig. 1b and Extended Data Table 2) in a concentration-dependent manner. Addition of SBI-553 with NTS further increased the interaction of NTSR1 with GRK2 or β-arrestin-2

(Fig. 1d,e, Extended Data Fig. 1b and Extended Data Table 2). Consistent with reports that SBI-553 is an arrestin-biased ligand⁷, SBI-553 alone promoted recruitment of β-arrestin-2 (Fig. 1b) but not of G_q protein (Fig. 1c), whereas NTS acted as a balanced ligand to promote recruitment of both arrestin and G_q protein (Fig. 1b,c).

Co-expression of NTSR1 with GRK2 as well as G_α_q and G_β_γ resulted in a complex that could be purified to homogeneity but was unstable (Extended Data Fig. 1c). We introduced the NanoBiT tethering strategy^{32,33} to stabilize the complex by fusing LgBiT to the C terminus of NTSR1 and HgBiT to the C terminus of GRK2. In addition, we added staurosporine and GDP-AlF₄⁻-Mg²⁺ to stabilize the NTSR1-GRK2-G_α_q complex. Staurosporine is an ATP-mimicking kinase inhibitor that can stabilize GRK2 in the active conformation, which is required for stable interaction with the active state of GPCRs^{34–37}. GDP-AlF₄⁻-Mg²⁺ mimics GTP, stabilizing G_α_q in the active conformation, which is required for stable interaction with GRK2¹⁸. The purification of the above complex showed a sub-stoichiometric ratio of the G_β_γ subunit (Extended Data Fig. 1d), indicating an instable association of the G_β_γ subunit with the rest of the complex. We thus omitted the G_β_γ subunit from the final complex assembly, which was further stabilized by chemical crosslinking with BS₃ for cryo-EM studies (Extended Data Fig. 1e–g).

A total of 57,477 images were collected, which yielded around 40 million initial particles. Further 2D classification and refinement generate two maps for two distinct NTSR1-GRK2-G_α_q complexes (hereafter referred to as complexes 1 and 2), both at global nominal resolutions of 3.1 Å (Extended Data Fig. 2). Local refinement of the NTSR1 (contains

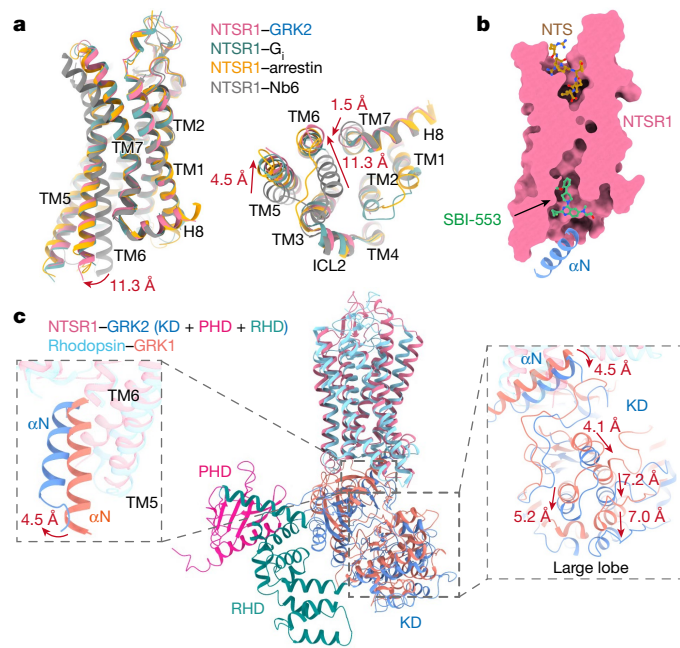


Fig. 2 | Structural features of the NTSR1-GRK2- $\text{G}\alpha_q$ complex. **a**, Structural comparison of NTSR1 from the NTSR1-GRK2- $\text{G}\alpha_q$ complex with inactive NTSR1 (PDB code: 7UL2), NTSR1 from the NTSR1-arrestin-2 complex (PDB code: 6UP7) and NTSR1 from the NTSR1- G_i complex (PDB code: 6OS9). **b**, The overall arrangement of the NTS and SBI-553 binding pockets in NTSR1. **c**, Structural comparison of the NTSR1-GRK2- $\text{G}\alpha_q$ complex with the rhodopsin-GRK1 complex (PDB code: 7MTA). KD, kinase domain.

a partial of GRK2), GRK2 bound with $\text{G}\alpha_q$ and $\text{G}\alpha_q$ alone from complex 1 yielded maps at resolutions of 2.9 Å, 2.8 Å and 3.0 Å, respectively (Extended Data Fig. 2). The statistics of cryo-EM data and structures are summarized in Extended Data Table 1. The maps for complexes 1 and 2 were both sufficiently clear to place NTSR1, NTS, GRK2, $\text{G}\alpha_q$ and the bound SBI-553, staurosporine and GDP- $\text{AlF}_4^- \cdot \text{Mg}^{2+}$ (Fig. 1f,g and Extended Data Fig. 3). Because the elongated shape of the NTSR1-GRK2- $\text{G}\alpha_q$ complex, the maps for NTSR1 extracellular segments and $\text{G}\alpha_q$ were less clear than the map for GRK2. Correspondingly, the residues with poor map density were built without side chains. The model building details are provided in Supplementary Tables 1–6. Comparison of these two complexes reveals that they have very similar NTSR1 structures (root mean squared deviation (r.m.s.d.) = 0.764 Å for the Cα atoms of the entire receptor) but a swing of GRK2 of approximately 5–6 Å compared with NTSR1 (Extended Data Fig. 4), suggesting the dynamics of the NTSR1-GRK2 complex assembly. 3D variability analysis (3DVA) of the two cryo-EM maps also reveal a dynamic swing of GRK2 around NTSR1, especially in the $\text{G}\alpha_q$ subunit and the relative positions between the RHD and kinase domain (Supplementary Video). Owing to the similarities between complexes 1 and 2, we focused our subsequent analysis on complex 1.

Structure of the NTSR1-GRK2-SBI-553 complex

Within the complex structure, NTSR1 resembles the NTSR1 structure in complex with G_i and β -arrestin^{23,24,30} (Fig. 2a), with more similarity to the NTSR1- G_i complex (r.m.s.d. of 0.725 Å for all Cα atoms of NTSR1). Compared with the inactive NTSR1 structure, conformational changes occurred mainly at cytoplasmic ends of TM5 (4.5 Å shift), TM6 (11.3 Å shift) and TM7 (1.5 Å shift), consistent with an active conformation of NTSR1 (Fig. 2a). In addition, ICL2 of NTSR1 in the NTSR1-GRK2- $\text{G}\alpha_q$ complex adopts an α -helical structure, a commonly observed property of GPCRs in their active conformations, further indicating that

GRK-GPCR engagement requires that the receptor is in the active state (Fig. 2a).

On the extracellular side, the peptide ligand NTS is fit into the top central transmembrane domain pocket (Fig. 2b) in a similar conformation to the previous NTS structures with NTSR1³⁸. At the intracellular side, SBI-553 is found at the NTSR1 cytoplasmic pocket to interact with the N-terminal helix of GRK2, which docks into the open cytoplasmic pocket of NTSR1 below SBI-553. The overall structure of the NTSR1-GRK2 complex is similar to the rhodopsin-GRK1 complex¹³ (Fig. 2c); however, the position of the N-terminal helix of GRK2 tilts by as much as 4.5 Å relative to the N-terminal helix of GRK1 (Fig. 2c). Correspondingly, the whole kinase domain of GRK2 tilts by as much as 6–7 Å from the GRK1 kinase domain (Fig. 2c).

Compared with the partial GRK1 structure in the rhodopsin-GRK1 complex, GRK2 from the NTSR1-GRK2 complex has a nearly complete structure with its RHD and PHD clearly defined in the structure (Fig. 2c). In the structure, $\text{G}\alpha_q$ is bound to the RHD of GRK2 (Extended Data Fig. 5). Comparing the GRK2 structure from the complex with NTSR1 with the crystal structure of GRK2 from the complex with $\text{G}\alpha_q$ and $\text{G}\beta\gamma$ reveals three major differences¹⁸ (Extended Data Fig. 5). The GRK2 structure from the NTSR1 complex contains a N-terminal helix that is packed onto the kinase domain (Extended Data Fig. 5), has a breakage in the ionic lock between its RHD from the kinase domain, and adopts a closed conformation in its kinase domain that is in the active state (Extended Data Fig. 5). By contrast, the GRK2 crystal structure from the complex with $\text{G}\alpha_q$ and $\text{G}\beta\gamma$ does not have the N-terminal helix, contains the ionic lock between its RHD and the kinase domain as seen in the GRK5 structures^{16,39}, and adopts an open conformation in its kinase domain, resembling the inactive state (Extended Data Fig. 5). Thus, the GRK2 structure in the NTSR1 complex is in the active state with its N-terminal helix packed against the GRK2 kinase domain, consistent with GRK2 being activated by binding to the active NTSR1.

The overall arrangement of the NTSR1-GRK2 complex also presents possible association of GRK2 with the membrane lipid layer (Extended Data Fig. 6a). Alignment of helix 8 (H8) of NTSR1 with the membrane layer reveals that the C-terminal tip of helix 9 from RHD and the N-terminal loop between β -strands 1 and 2 from the PHD are in close contact with the membrane layer (Extended Data Figs. 6a and 7). This region is homologous to the C-terminal lipid binding domain (CLBD) of GRK5¹⁶. GRK2 also contains the homologous region to the N-terminal lipid binding domain (NLBD) of GRK5, and the structure of the NTSR1-GRK2 complex reveals that both NLBD and CLBD are near the membrane layer. These regions are enriched with positively charged residues that could engage interactions with the negatively charged lipid membrane. Alanine mutations of these basic residues reduced recruitment of GRK2 to NTSR1 (Extended Data Fig. 6b and Extended Data Table 3). Additional binding of GRK2 to the membrane layer could come from lipid modifications at cysteine 9 and cysteine 10 of $\text{G}\alpha$ and cysteine 68 of $\text{G}\beta$ subunits (Extended Data Fig. 6a), and these lipid modifications could further facilitate GRK2 membrane binding^{40,41}.

The GRK2-NTSR1 interface

The GRK2-NTSR1 interface is at the centre of the complex, with a clear density map that reveals detailed intermolecular interactions between GRK2 and NTSR1 at the residue-specific level (Fig. 3 and Extended Data Fig. 3). The GRK2-NTSR1 complex has a major interface consisting of the N-terminal helix of GRK2, which inserts into the open TM6 pocket (Fig. 3a,b) and a minor interface consisting of ICL2 of NTSR1, that interacts with the loop between the N-terminal helix and the RHD (Fig. 3c).

At the major interface, five hydrophobic residues (L4, V7, L8, V11 and M15) from the N-terminal helix of GRK2 form an extended hydrophobic patch, which is packed against a hydrophobic pocket formed by hydrophobic residues from TM5 and TM6 (L263^{5,65}, M266^{5,68}, A297^{6,29}, L298^{6,30} and G301^{6,33}, using the Ballesteros-Weinstein numbering

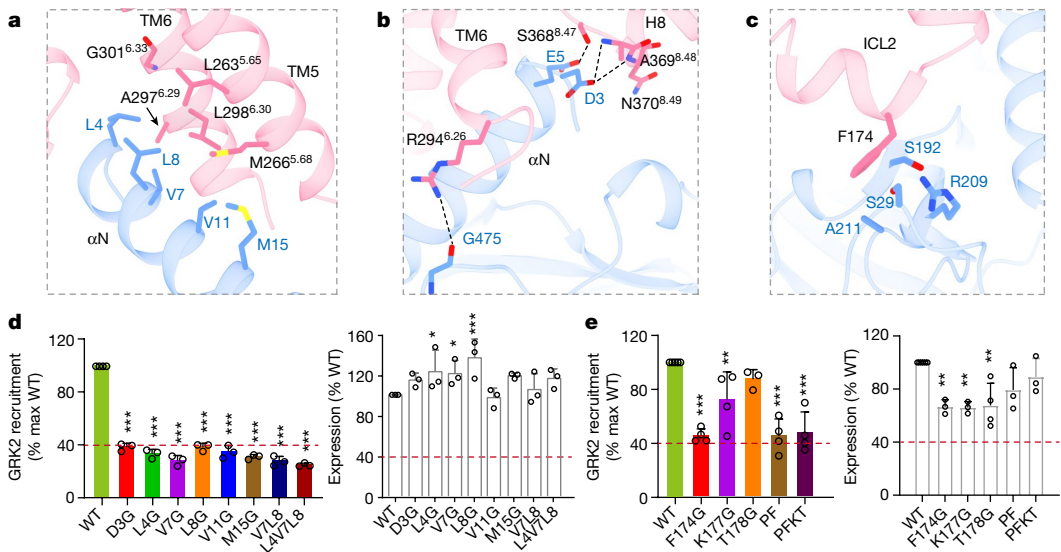


Fig. 3 | Interactions between NTSR1 and GRK2. **a,b**, Detailed interactions at the major interface between the NTSR1 cytoplasmic hydrophobic pocket and GRK2. Hydrophobic interactions between NTSR1 and GRK2 (**a**), hydrophilic interactions between NTSR1 and GRK2 (**b**). **c**, Detailed interactions at the minor interface between NTSR1 ICL2 and GRK2. NTSR1 is shown in pink and GRK2 is shown in blue. The cut-off distance used to determine interactions is 4.0 Å. **d**, Recruitment of wild-type (WT) and N-terminal-mutated GRK2 to NTSR1 induced by NTS (left) and the relative expression level of wild-type and

N-terminal-mutated GRK2 (right). Data are mean ± s.d. from three independent experiments ($n = 3$). **e**, GRK2 recruitment to wild-type and ICL2-mutated receptors induced by NTS (left) and relative expression level of wild-type and ICL2-mutated receptors (right). V7L8, V7G/L8G; L4V7L8, L4G/V7G/L8G; PF, P173G/F174G; PFKT, P173G/F174G/K177G/T178G. Data are mean ± s.d. from at least three independent experiments ($n \geq 3$). Two-sided one-way ANOVA was used for differences between wild type and mutants. * $P < 0.05$, ** $P < 0.01$ and *** $P < 0.001$. Detailed information is provided in Extended Data Table 3.

system) (Fig. 3a). In addition, the carboxylate side chain of D3 of GRK2 forms a network of hydrogen bonds with the main chain amine groups of N370^{8.49} and A369^{8.48} from NTSR1. The carboxylate side chain of E5 of GRK2 forms a hydrogen bond with the side chain of S368^{8.47}. R294^{6.26} also forms a direct hydrogen bond with the main chain carbonyl from G475 of GRK2 (Fig. 3b). These additional hydrogen bonds may also help to stabilize the N-terminal helix of GRK2 in the cytoplasmic pocket. Consistent with their role in the NTSR1–GRK2 interactions, alanine mutations of most interface residues resulted in significant reductions in GRK2 recruitment to NTSR1 (Fig. 3d and Extended Data Table 3).

At the ICL2 minor interface, only F174 is packed against the side chains of S29, S192, R209 and A211 from GRK2 (Fig. 3c). F174G mutation either alone or combined with other residues from the ICL2 helix (PF and PFKT mutations; Fig. 3e) had similar expression levels to the wild-type receptor with F174G. Notably, the PF or PFKT mutations in combination with F174G had similar effects to the F174G mutation alone on the reduction of GRK2 recruitment to NTSR1 (Fig. 3e and Extended Data Table 3), indicating that F174 is the critical residue involved in the ICL2–GRK2 interaction. It should also be noted that F174 is critical for G_q engagement³⁰. The total buried surface area between GRK2 and NTSR1 is 746 Å², which is considerably smaller than the NTSR1–G_i interface area (1,197 Å²), consistent with the relatively weak NTSR1–GRK2 interactions.

The basis of SBI-553 biased agonism

SBI-553 is an arrestin-biased PAM ligand that specifically blocks G_q protein signalling but enhances arrestin signalling⁷. The high-quality density map clearly defines the binding mode of SBI-553 (Fig. 4), which adopts an inverted T-shaped configuration and binds to the interface between NTSR1 and GRK2 (Fig. 4a,b). In the structure, SBI-553 forms extensive interactions with both receptor and GRK2 as summarized in Supplementary Table 7. Specifically, with NTSR1, SBI-553 forms predominantly hydrophobic interactions with residues from TM2, TM3, TM5, TM6, TM7 and H8, including L162^{3.46}, L305^{6.37} and V367^{7.56} (Fig. 4c,d). With GRK2, SBI-553 forms direct interactions with L4, E5 and

L8 from the N-terminal helix (Fig. 4d), consistent with the enhanced binding of GRK2 to NTSR1 by SBI-553 (Fig. 1d). To demonstrate the direct effects of GRK2 recruitment by SBI-553, we mutated receptors with larger side chains (L162F/W, L305W/Y and V367F/Y), which were designed to protrude into the SBI-553-binding pocket. Consistently, receptors with L162F or L305W mutations, which did not have major effects on receptor expression, resulted in reduced ability of SBI-553 to induce GRK2 recruitment (Fig. 4e,f and Extended Data Table 3).

The binding site of SBI-553 is unique and has not been observed in any GPCR structures determined to date^{42,43}. Structure superposition of NTSR1 from the complex with G_q onto the NTSR1–GRK2 structure reveals that the α5 helix of the G proteins occupies roughly the same space as occupied by the N-terminal helix of GRK2 (Fig. 4g). In this orientation, the α5 helix from the G_q would clash directly with the bound SBI-553 (Fig. 4g), thus providing a direct explanation for the inhibition of G_q protein signalling by SBI-553. By contrast, structural superposition of NTSR1 from the complex with arrestin reveals that the binding of SBI-553 would be compatible with arrestin binding to NTSR1 (Fig. 4i), consistent with its arrestin-biased signalling property. During the review of our paper⁴⁴, it was reported that SBI-553 binding could result in a shift in the orientation of the C-terminal α5 helix of the G_{q/o} protein but not that of G_q, leading to SBI-553 bound NTSR1 being able to selectively couple with G_{i/o} protein but not with G_q⁴⁵ (Fig. 4h), further indicating that SBI-553 is not only biased for arrestin, but also selective for G_{i/o} over G_q.

Universal features of GPCR–GRK interactions

Here we have determined the structure of NTSR1 in complex with GRK2 and SBI-553 at a resolution of 3.1 Å (Extended Data Fig. 2d). The structure shows a clear binding mode of GRK2 and SBI-553 to NTSR1 as well as the mode of GRK2 membrane association. The primary binding site of GRK2 at NTSR1 overlaps with the NTSR1 G-protein binding site composed of ICL2, TM6, TM7 and H8, features that are highly similar in the active structures of various GPCRs (Extended Data Fig. 8), thus providing a basis for the ability of GRK2 to interact with many different GPCRs.

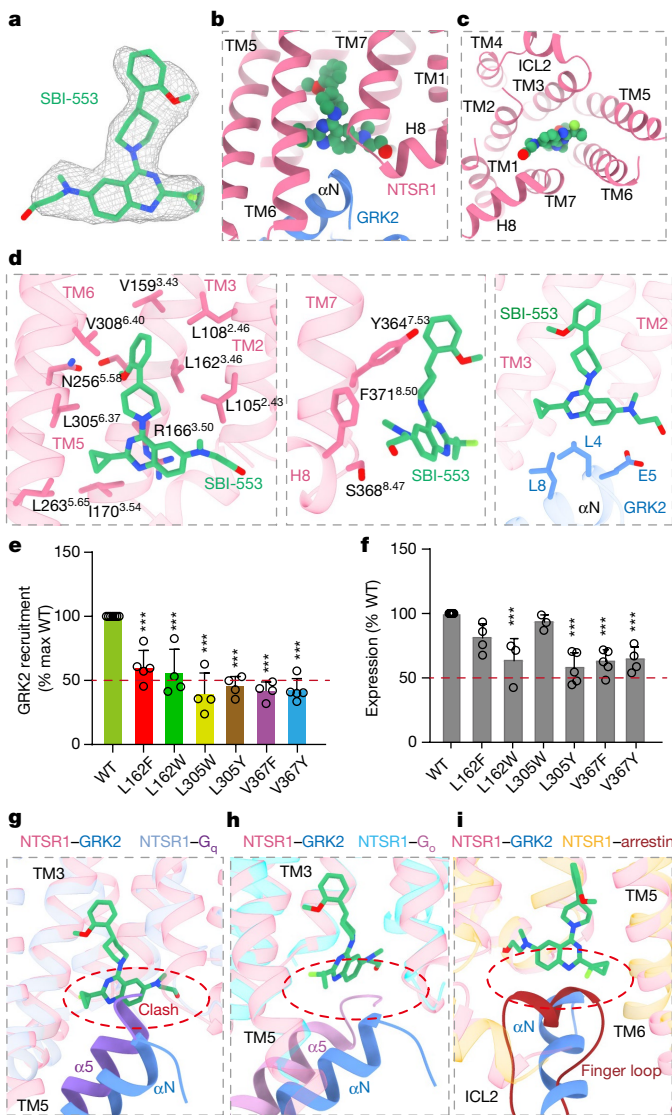


Fig. 4 | The binding mode of SBI-553 in NTSR1. **a**, Electron microscopy density of SBI-553, which is shown at a level of 0.25. **b,c**, The binding pocket of SBI-553 in NTSR1, in front view (**b**) and bottom view (**c**) relative to the membrane plane. SBI-553 is highlighted in sphere view. **d**, Detailed interactions between SBI-553, NTSR1 and GRK2. SBI-553 is shown in green, NTSR1 is shown in pink, and GRK2 is shown in blue. **e,f**, GRK2 recruitment to wild-type and mutated receptors induced by NTS (**e**) and relative expression level of wild-type and mutated receptors (**f**). Data are mean \pm s.d. from at least 3 independent experiments ($n \geq 3$). Two-sided one-way ANOVA was used for differences between wild type and mutants. Detailed information is provided in Extended Data Table 3. **g**, Superposition of NTSR1 from NTSR1–GRK2–G α_q and NTSR1–G α_q complexes (PDB ID: 8FMZ) shows that α_5 of G α_q would clash with SBI-553. **h**, Superposition of NTSR1 from NTSR1–GRK2–G α_q and NTSR1–G α_i complexes (PDB ID: 8FNO) shows that α_5 of G α_i is compatible with SBI-553 binding. **i**, Superposition of NTSR1 from the NTSR1–GRK2–G α_q complex and the NTSR1–arrestin complex (PDB: 6UP7) shows that the finger loop of arrestin is compatible with the location of SBI-553.

In addition, the GRK2 binding site on NTSR1 is similar to the GRK1 binding site in rhodopsin (Fig. 2c). In our structure, GRK2 is nearly complete, with clear definition of many flexible regions, including the RHD and the active site tether (AST) loop, which tethers the kinase domain in the active conformation. The residues from the N-terminal helix of GRK2 that interact with NTSR1 are highly conserved in all GRKs, suggesting that the binding mode of GRK2 is a universal feature of all GRKs (Extended Data Fig. 7).

The NTSR1–GRK2 complex structure could also facilitate a mechanistic understanding of GRK activation and possible substrate recognition of the GPCR C terminus or ICL3 by GRK2. Uncoupled GRKs are inactive and the N-terminal region is unstructured in all inactive GRK structures^{39,46}. Upon binding to the active NTSR1, the N-terminal region of GRK2 adopts a helix within the GPCR cytoplasmic pocket and is packed against the GRK2 kinase domain, which stabilizes the kinase domain in the active conformation. These structural observations support the activation of GRK2 by binding to the active NTSR1. Also based on the NTSR1–GRK2 complex structures, the extended loop of ICL3 or the elongated C-terminal tail of the GPCR could reach the active cleft of GRK2 (Extended Data Fig. 6c) and thus be available for phosphorylation by GRK2. By contrast, ICL1 and ICL2 of the GPCR is unlikely to be accessible to the kinase active site in the complex, possibly explaining why there are few phosphorylation sites in ICL1 and ICL2.

Finally, our structure reveals an unexpected binding mode of SBI-553, which is docked at the interface between GRK2 and NTSR1, consistent with its ability to enhance GRK2 binding to NTSR1 (Fig. 1a,d). The binding of SBI-553 is compatible with arrestin binding but would clash with G α binding (Fig. 4g,h), thus providing a direct mechanism for its arrestin-biased signalling capability (Extended Data Fig. 9). Combined with recent data⁴⁵ showing that SBI-553-bound NTSR1 is permissive for coupling with G i/o , our study reveals that SBI-553 is both biased towards arrestin signalling and selective for G i/o binding.

G protein- or arrestin-biased ligands have become a recent focus of GPCR drug discovery studies. Because GRK is the key regulator that determines the switch of GPCRs from G-protein signalling to arrestin signalling, the structure of the GPCR–GRK complex is highly relevant for the design of drugs based on biased ligands. Furthermore, the binding site of SBI-553 provides a direct target on which small molecules that can selectively modulate the binding of G protein, GRK and arrestin can be designed, thus opening a new area for GPCR drug discovery. In sum, our structure provides a model for understanding the details of GPCR–GRK interactions and GRK2-mediated signalling, and a basis for designing biased ligands such as SBI-553 derivatives for NTSR1 and possibly other GPCRs.

Online content

Any methods, additional references, Nature Portfolio reporting summaries, source data, extended data, supplementary information, acknowledgements, peer review information; details of author contributions and competing interests; and statements of data and code availability are available at <https://doi.org/10.1038/s41586-023-06395-9>.

- Pitcher, J. A., Freedman, N. J. & Lefkowitz, R. J. G protein-coupled receptor kinases. *Annu. Rev. Biochem.* **67**, 653–692 (1998).
- Gurevich, E. V., Tesmer, J. J., Mushegian, A. & Gurevich, V. V. G protein-coupled receptor kinases: more than just kinases and not only for GPCRs. *Pharmacol. Ther.* **133**, 40–69 (2012).
- Gurevich, V. V. & Gurevich, E. V. GPCR signaling regulation: the role of GRKs and arrestins. *Front. Pharmacol.* **10**, 125 (2019).
- Hodavance, S. Y., Gareci, C., Torok, R. D. & Rockman, H. A. G protein-coupled receptor biased agonism. *J. Cardiovasc. Pharmacol.* **67**, 193–202 (2016).
- Rankovic, Z., Brust, T. F. & Bohn, L. M. Biased agonism: an emerging paradigm in GPCR drug discovery. *Bioorg. Med. Chem. Lett.* **26**, 241–250 (2016).
- Seyedabadi, M., Gharghabi, M., Gurevich, E. V. & Gurevich, V. V. Structural basis of GPCR coupling to distinct signal transducers: implications for biased signaling. *Trends Biochem. Sci.* **47**, 570–581 (2022).
- Slosky, L. M. et al. β -Arrestin-biased allosteric modulator of NTSR1 selectively attenuates addictive behaviors. *Cell* **181**, 1364–1379.e1314 (2020).
- Benovic, J. L., DeBlasi, A., Stone, W. C., Caron, M. G. & Lefkowitz, R. J. β -Adrenergic receptor kinase: primary structure delineates a multigene family. *Science* **246**, 235–240 (1989).
- Mushegian, A., Gurevich, V. V. & Gurevich, E. V. The origin and evolution of G protein-coupled receptor kinases. *PLoS ONE* **7**, e3806 (2012).
- Sulon, S. M. & Benovic, J. L. Targeting G protein-coupled receptor kinases (GRKs) to G protein-coupled receptors. *Curr. Opin. Endocr. Metab. Res.* **16**, 56–65 (2021).
- Ribas, C. et al. The G protein-coupled receptor kinase (GRK) interactome: role of GRKs in GPCR regulation and signaling. *Biochim. Biophys. Acta* **1768**, 913–922 (2007).

12. Komolov, K. E. et al. Structure of a GRK5–calmodulin complex reveals molecular mechanism of GRK activation and substrate targeting. *Mol. Cell* **81**, 323–339 e311 (2021).
13. Chen, Q. et al. Structures of rhodopsin in complex with G-protein-coupled receptor kinase 1. *Nature* **595**, 600–605 (2021).
14. Beaupain, A. et al. Mapping the putative G protein-coupled receptor (GPCR) docking site on GPCR kinase 2: insights from intact cell phosphorylation and recruitment assays. *J. Biol. Chem.* **289**, 25262–25275 (2014).
15. Baameur, F. et al. Role for the regulator of G-protein signaling homology domain of G protein-coupled receptor kinases 5 and 6 in beta 2-adrenergic receptor and rhodopsin phosphorylation. *Mol. Pharmacol.* **77**, 405–415 (2010).
16. Komolov, K. E. et al. Structural and functional analysis of a β_2 -adrenergic receptor complex with GRK5. *Cell* **169**, 407–421.e416 (2017).
17. Loduski, D. T., Pitcher, J. A., Capel, W. D., Lefkowitz, R. J. & Tesmer, J. J. Keeping G proteins at bay: a complex between G protein-coupled receptor kinase 2 and G β . *Science* **300**, 1256–1262 (2003).
18. Tesmer, V. M., Kawano, T., Shankaranarayanan, A., Kozasa, T. & Tesmer, J. J. Snapshot of activated G proteins at the membrane: the G α_q –GRK2–G β complex. *Science* **310**, 1686–1690 (2005).
19. He, Y. et al. Molecular assembly of rhodopsin with G protein-coupled receptor kinases. *Cell Res.* **27**, 728–747 (2017).
20. Rasmussen, S. G. et al. Crystal structure of the β , adrenergic receptor–G $_s$ protein complex. *Nature* **477**, 549–555 (2011).
21. Kang, Y. et al. Crystal structure of rhodopsin bound to arrestin by femtosecond X-ray laser. *Nature* **523**, 561–567 (2015).
22. Zhou, X. E. et al. Identification of phosphorylation codes for arrestin recruitment by G protein-coupled receptors. *Cell* **170**, 457–469.e413 (2017).
23. Yin, W. et al. A complex structure of arrestin-2 bound to a G protein-coupled receptor. *Cell Res.* **29**, 971–983 (2019).
24. Huang, W. et al. Structure of the neuropeptide receptor 1 in complex with β -arrestin 1. *Nature* **579**, 303–308 (2020).
25. Staus, D. P. et al. Structure of the M2 muscarinic receptor– β -arrestin complex in a lipid nanodisc. *Nature* **579**, 297–302 (2020).
26. Lee, Y. et al. Molecular basis of β -arrestin coupling to formoterol-bound β_2 -adrenoceptor. *Nature* **583**, 862–866 (2020).
27. Besserer-Offroy, E. et al. The signaling signature of the neuropeptide receptor type 1 receptor with endogenous ligands. *Eur. J. Pharmacol.* **805**, 1–13 (2017).
28. Rostene, W. H. & Alexander, M. J. Neuropeptide and neuroendocrine regulation. *Front. Neuroendocrinol.* **18**, 115–173 (1997).
29. Inagaki, S. et al. G protein-coupled receptor kinase 2 (GRK2) and 5 (GRK5) exhibit selective phosphorylation of the neuropeptide receptor in vitro. *Biochemistry* **54**, 4320–4329 (2015).
30. Kato, H. E. et al. Conformational transitions of a neuropeptide receptor 1–G $_i$ complex. *Nature* **572**, 80–85 (2019).
31. Barnea, G. et al. The genetic design of signaling cascades to record receptor activation. *Proc. Natl Acad. Sci. USA* **105**, 64–69 (2008).
32. Dixon, A. S. et al. NanoLuc complementation reporter optimized for accurate measurement of protein interactions in cells. *ACS Chem. Biol.* **11**, 400–408 (2016).
33. Duan, J. et al. Cryo-EM structure of an activated VIP1 receptor–G protein complex revealed by a NanoBIT tethering strategy. *Nat. Commun.* **11**, 4121 (2020).
34. Cato, M. C. et al. The open question of how GPCRs interact with GPCR kinases (GRKs). *Biomolecules* **11**, 447 (2021).
35. Homan, K. T. & Tesmer, J. J. Molecular basis for small molecule inhibition of G protein-coupled receptor kinases. *ACS Chem. Biol.* **10**, 246–256 (2015).
36. Pellegrini, E., Signor, L., Singh, S., Boeri Erba, E. & Cusack, S. Structures of the inactive and active states of RIP2 kinase inform on the mechanism of activation. *PLoS ONE* **12**, e0177161 (2017).
37. Underwood, K. W. et al. Catalytically active MAP KAP kinase 2 structures in complex with staurosporine and ADP reveal differences with the autoinhibited enzyme. *Structure* **11**, 627–636 (2003).
38. White, J. F. et al. Structure of the agonist-bound neuropeptide receptor. *Nature* **490**, 508–513 (2012).
39. Komolov, K. E., Bhardwaj, A. & Benovic, J. L. Atomic structure of GRK5 reveals distinct structural features novel for G protein-coupled receptor kinases. *J. Biol. Chem.* **290**, 20629–20647 (2015).
40. Pitcher, J. A. et al. Role of β subunits of G proteins in targeting the β -adrenergic receptor kinase to membrane-bound receptors. *Science* **257**, 1264–1267 (1992).
41. Smrcka, A. V. G protein β subunits: central mediators of G protein-coupled receptor signaling. *Cell. Mol. Life Sci.* **65**, 2191–2214 (2008).
42. Draper-Joyce, C. J. et al. Positive allosteric mechanisms of adenosine A1 receptor-mediated analgesia. *Nature* **597**, 571–576 (2021).
43. Egyed, A., Kiss, D. J. & Keseru, G. M. The impact of the secondary binding pocket on the pharmacology of class A GPCRs. *Front. Pharmacol.* **13**, 847788 (2022).
44. Duan, J. et al. Structure of a G protein-coupled receptor with GRK2 and a biased ligand. Preprint at *bioRxiv* <https://doi.org/10.1101/2022.10.19.512855> (2022).
45. Krumm, B. E. et al. Neuropeptide receptor allosterism revealed in complex with a biased allosteric modulator. *Biochemistry* **62**, 1233–1248 (2023).
46. Bouley, R. A. et al. A new paroxetine-based GRK2 inhibitor reduces internalization of the μ -opioid receptor. *Mol. Pharmacol.* **97**, 392–401 (2020).

Publisher's note Springer Nature remains neutral with regard to jurisdictional claims in published maps and institutional affiliations.

Springer Nature or its licensor (e.g. a society or other partner) holds exclusive rights to this article under a publishing agreement with the author(s) or other rightsholder(s); author self-archiving of the accepted manuscript version of this article is solely governed by the terms of such publishing agreement and applicable law.

© The Author(s), under exclusive licence to Springer Nature Limited 2023

Methods

Constructs

Human NTSR1 (residues 1–418) was codon-optimized for expression in sf9 cells and cloned into a modified pFastBac vector, which contains an N-terminal hemagglutinin (HA) signal peptide followed by a Flag tag and a b562RIL epitope before the receptor. To improve the complex homogeneity and stability, the NanoBiT tethering strategy was applied by fusing a LgBiT subunit (Promega) at the receptor C terminus after a GSSGGSGGGG linker^{32,33}. Bovine GRK2 was cloned with a C-terminal GSSGGSGGGG linker followed by the HiBiT (peptide86) subunit³³. Additionally, three mutations (A292P, R295I and S455D) were incorporated into GRK2 by site-directed mutagenesis to enhance the affinity between GRK2 and Fab6¹³. Gα_q construct was modified into a pFastBac vector and the native N terminus (residues 1–28) of Gα_q was replaced with Gα₁ to facilitate the expression of Gα_q¹⁸. Human embryonic kidney 293T (HEK293) cells were obtained from ATCC (CRL-3216). HTL cells were a gift from G. Barnea and R. Axel (Brown University and Columbia University). Hi5 cells were purchased from Invitrogen (B85502). All the cell lines used in this study were maintained by the supplier and no additional authentication was performed by the authors. All the cell lines were negative for mycoplasma contamination.

Expression and purification of the NTSR1–GRK2–Gα_q complex

NTSR1–LgBiT, Gα_q, GRK2–HiBiT and Ric8a (a gift from B. Kobilka) were co-expressed in Hi5 insect cells (Invitrogen) using the Bac-to-Bac baculovirus expression system (ThermoFisher). Cell pellets were thawed and lysed in 20 mM HEPES, pH 7.4, 100 mM NaCl, 10% glycerol, 10 mM MgCl₂, 10 mM NaF and 30 μM AlCl₃ supplemented with Protease Inhibitor Cocktail, EDTA-Free (TargetMol). The NTSR1–GRK2–Gα_q complex was formed in membranes by the addition of 10 μM NTS (Genscript), 10 μM staurosporine, 10 μM SBI-553 (TargetMol) and 50 μM GDP. The suspension was incubated for 0.5 h at room temperature before centrifugation at 80,000g for 30 min. The membrane was then resuspended with the same buffer and solubilized using 0.5% (w/v) *n*-dodecyl-β-D-maltoside (DDM) (Anatrace), 0.1% (w/v) cholesterol hemisuccinate (CHS) (Anatrace) for 2 h at 4 °C. The supernatant was collected by centrifugation at 80,000g for 40 min and then incubated with G1 anti-Flag affinity resin (Genscript) for 2 h at 4 °C. After batch binding, the resin was loaded into a plastic gravity flow column and washed with 20 column volumes of 20 mM HEPES, pH 7.4, 100 mM NaCl, 10% glycerol, 10 mM MgCl₂, 10 mM NaF, 30 μM AlCl₃, 10 μM NTS, 10 μM staurosporine, 10 μM SBI-553 and 50 μM GDP, 0.01% (w/v) DDM, 0.002% (w/v) CHS, and 0.05% (w/v) digitonin, further eluted with 10 column volumes of the same buffer plus 0.2 mg ml⁻¹ Flag peptide. The complex was then concentrated using an Amicon Ultra Centrifugal Filter (MWCO 100 kDa) and injected onto a Superose 6 Increase 10/300 GL column (GE Healthcare) equilibrated in the buffer containing 20 mM HEPES, pH 7.4, 100 mM NaCl, 10 mM MgCl₂, 10 mM NaF, 30 μM AlCl₃, 10 μM NTS, 10 μM staurosporine, 5 μM SBI-553, 50 μM GDP, and 0.03% (w/v) digitonin. To stabilize the NTSR1–GRK2–Gα_q complex, the peak fractions were collected and crosslinked using 0.01 mM BS₃ for 0.5 h at room temperature, stopped crosslinking by addition of 80 mM of glycine, and then concentrated to approximately 10 mg ml⁻¹ for cryo-EM analysis.

Cryo-EM grid preparation and data collection

For the preparation of cryo-EM grids, 3 μl of the purified protein at 10 mg ml⁻¹ were applied onto a glow-discharged holey carbon grid (CryoMatrix Amorphous alloy film R1.2/1.3, 300 mesh). Grids were plunge-frozen in liquid ethane using Vitrobot Mark IV (Thermo Fischer Scientific). Frozen grids were transferred to liquid nitrogen and stored for data acquisition. Cryo-EM imaging of the complex was performed on a Titan Krios G4 at 300 kV in the Advanced Center for Electron Microscopy at Shanghai Institute of Materia Medica, Chinese Academy of Sciences.

A total of 57,477 movies for the NTSR1–GRK2–Gα_q complex were collected by a Gatan K3 Summit direct electron detector with a Gatan energy filter (operated with a slit width of 20 eV) (GIF) at a pixel size of 0.824 Å using the EPU software. The movies were recorded in super-resolution mode and were obtained at a dose rate of about 15 e⁻ Å² s⁻¹ with a defocus ranging from −1.2 to −2.2 μm. The total exposure time was 2.35 s with a total dose of 50 electrons, resulting in a total of 36 frames per micrograph.

Image processing and map construction

A total of 57,477 dose-fractionated movies were used for correction of beam-induced movement using a dose-weighting scheme in MotionCor²⁴⁷ and their contrast transfer function parameters were estimated by Patch CTF estimation in CryoSPARC⁴⁸. For the NTSR1–GRK2–Gα_q complex, particle selection was performed by blob picking using CryoSPARC⁴⁸, and 40,940,867 particles were extracted and further subjected to an initial reference-free 2D classification. Interactive 2D classifications were performed to discard poorly defined particles, and 1,149,932 particles were retained. These particles were divided into 6 subclasses using ab-initio model and hetero-refinement, resulting in two subsets with complete NTSR1–GRK2–Gα_q complex. Two maps from the two subsets showed slight differences, especially relative position of GRK2 and Gα_q. We use one of the maps to generate 2D references to re-pick particles from 55,688 micrographs that have removed disposable movies. A total of 80,825,912 particles we extracted 1,205,682 particles, which were divided into five subclasses, were generated after further interactive 2D classifications. In the 5 subclasses, two subsets were well-defined, with one of the subsets containing 474,232 particles was subsequently subjected to non-uniform refinement. In order to improve resolution, a mask of complex 1 without micelle was applied to do particle subtraction and local refinement and generated a map with global resolution of 3.08 Å (complex 1) in CryoSPARC⁴⁸. In addition, masks created from each portion of the complex 1, including receptor, GRK2 bound with Gα_q and only Gα_q, respectively, were subjected for further particle subtraction and local refinement. The mask focusing on the receptor preserved part of the GRK2 density for alignment and generated a local map at resolution of 2.91 Å. Local refinement focusing on GRK2 bound with Gα_q and only Gα_q generated local maps at resolution of 2.81 Å and 3.02 Å, respectively. The other subset was performed another round of ab initio model and hetero-refinement to remove bad particles, and one well-defined subset with 233,943 particles was subjected to non-uniform refinement and generated a map with global resolution of 3.10 Å (complex 2). Resolution was estimated in the presence of a soft solvent mask and based on the gold standard Fourier shell correlation (FSC) 0.143 criterion. Local resolution was estimated in cryoSPARC⁴⁸ using default parameters.

To analyse the flexibility of the NTSR1–GRK2–Gα_q complex, we performed 3DVA in cryoSPARC⁴⁹. The 3DVA was performed with mask on the complex, generated from non-uniform refinement. The 3DVA was analysed across three principal components that estimated the most common motions. One of the components showed pronounced motion between GRK2 and Gα_q and the movie that consisted of 20 volume frame data are presented using Chimera (v1.4) in the Supplementary Video.

Model building and refinement

For NTSR1–GRK2–Gα_q complex 1 and complex 2, the AlphaFold model of NTSR1, the structure of the NTS–NTSR1 complex (PDB code: 4RGV), and GRK2 in complex with Gα_q and Gβγ subunits (PDB code: 2BCJ), were used as the start for model building and refinement against the electron microscopy maps. For model building of NTSR1 and GRK2 of complex 1, the B-factor sharpened global map and the local density maps were used as the references, and for the model building of Gα_q of complex 1, the local density map focusing on Gα_q was used as the main reference. For model building of NTSR1–GRK2–G_q complex 2, the B-factor sharpened map was used as reference. The model was docked

into the two EM density maps using Chimera⁵⁰, respectively, followed by iterative manual adjustment and rebuilding in COOT⁵¹ and ISOLDE⁵². Real space and reciprocal space refinements were performed using Phenix⁵³ with secondary structure and geometry restraints. The final refinement statistics were validated using the module ‘comprehensive validation (cryo-EM)’ in Phenix⁵³. The details for the final model building of each section of the complexes and the side chains which are invisible in the density maps that were stubbed are listed in Supplementary Tables 1–6. The final refinement statistics are provided in Extended Data Table 1. Structure figures were prepared in ChimeraX⁵⁴ and PyMOL (<https://pymol.org/2/>).

Calculation of NTSR1–G_i and NTSR1–GRK2 interface area

NTSR1–GRK2–Gα_q and NTSR1–G_i (PDB ID: 6OS9) were used for the calculation of NTSR1–GRK2 and NTSR1–G_i interface areas, respectively, using the PDBePISA web server (<https://www.ebi.ac.uk/pdbe/pisa/>). During the process, NTSR1–GRK2–Gα_q complex and NTSR1–G protein complexes were uploaded, and the accessible surface area calculations are based on finite element analysis through the ‘interface’ module.

NanoBiT assay

The full-length NTSR1 (1–418) was cloned into pBiT1.1 vector (Invitrogen) with a Flag tag at its N terminus and LgBiT at its C terminus. Bovine GRK2 (residues 1–689), human β-arrestin-2 (residues 1–393, with mutations I386A, V387A and F388A) and bovine Gβ (residues 1–345) were cloned into pBiT2.1 vector (Invitrogen) with a modified SmBiT (peptide104: MVEGYRLFEKIS)³² and a GSSGGGGSGGGSSG linker at N terminus of GRK2 and β-arrestin-2, and C terminus of Gβ. Human Gα_q (wild type) and G_i (wild type) were also cloned into pBiT2.1 vector, respectively. HEK293T cells (3.2×10^6 cells per 10-cm dish) were grown for 24 h to reach 70% to 80% confluence. Then the cells were transiently transfected with 13 µg plasmids, with NTSR1–LgBiT (wild type or mutants) and SmBiT–GRK2 (wild type or mutants) at a ratio of 1:1 or NTSR1–LgBiT (wild type) and SmBiT–β-arrestin-2 at a ratio of 1:1, or NTSR1–LgBiT (wild type), Gβ–SmBiT, Gα_q and G_i at a ratio of 2:1:1:1 with Lipofectamine 3000 (Invitrogen) transfection reagent. Twenty-four hours after transfection, cells were seeded into poly-D-lysine-coated 96-well culture plates at a density of 5×10^4 cells per well in DMEM with 10% FBS and 1% (v/v) sodium pyruvate (Gibco). Cells were grown overnight before incubation in HBSS buffer (pH 7.4) supplemented with 0.1% BSA and 10 mM HEPES for 30 min at 37 °C (no CO₂). They were then reacted with coelenterazine H (5 µM) for 1.5 h, at room temperature. Luminescence signals were measured using an EnVision plate reader at 30-s intervals (25 °C). In brief, the plates were read for 3.5 min as baseline, then read for 10 min after addition of ligand. Data were corrected to baseline and vehicle-treated samples. The area under the curve (AUC) across the time-course response curve was determined and normalized to the NTS-induced GRK2 (wild type), β-arrestin-2 (residues 1–393, with mutations I386A, V387A and F388A) or Gβ recruitment to NTSR1 (wild type). Data were analysed using Graphpad Prism 9.0. Experiments were performed at least three times in duplicate and data were presented as mean ± s.d.

Detection of surface expression of NTSR1 mutants

The cell seeding and transfection followed the same method as the NanoBiT assay. Cells were seeded (6-well plate) and transiently transfected with 4 µg wild-type or mutated NTSR1 every hole. After 24 h of transfection, cells were washed once with PBS and then detached with 0.02% (w/v) EDTA in PBS. Cells were blocked with PBS containing 5% (w/v) BSA for 15 min at room temperature before incubating with primary anti-Flag M2 antibody (diluted with PBS containing 5% BSA at a ratio of 1:300, Sigma-Aldrich) for 1 h at room temperature. Cells were then washed 3 times with PBS containing 1% (w/v) BSA and then incubated with anti-mouse Alexa-488-conjugated secondary antibody (diluted at a ratio of 1:1,000, Invitrogen) at 4 °C in the dark for 1 h. After

another three times of washing, cells were collected, and fluorescence intensity was quantified in a BD Accuri C6 flow cytometer system (BD Biosciences) through a BD Accuri C6 software 1.0.264.21 at excitation 488 nm and emission 519 nm. Approximately 10,000 cellular events per sample were collected and data were normalized to the wild-type receptor. Data were analysed using Graphpad Prism 9.0. Experiments were performed at least three times and data were presented as mean ± s.d.

Detection of expression of GRK2 mutants

The cell seeding and transfection followed the same method as the NanoBiT assay. Cells were seeded (6-well plate) and transiently transfected with 4 µg wild-type or mutated GRK2. After 24 h of transfection, cellytic M reagent (Sigma-Aldrich) was added to each well and the plate was shaken for 30 min at 4 °C. Cell lysates were mixed with 5× SDS loading buffer and heated at 95 °C for 10 min. The samples were then loaded onto a protein gel transferred to PVDF membrane (Merck Millipore) for western blot analysis. The PVDF membrane was blocked with 1% BSA in TBST (20 mM Tris-HCl, pH 7.4, 150 mM NaCl, and 0.1% Tween 20) and incubated with flag tag mouse antibody (diluted at a ratio of 1:1,000, Abclonal) and rabbit β-tubulin antibody (diluted at a ratio of 1:5,000, Abclonal) followed by HRP-conjugated anti-mouse or anti-rabbit antibodies (diluted at a ratio of 1:10,000, Abclonal), respectively. Protein bands were detected by SuperSignal West Pico Chemiluminescent Substrate (Thermo Scientific), and images were collected using the ChemiDocTM XRS+ imager (Bio-Rad). ImageJ software was used to calculate the data. Data were analysed using Graphpad Prism 9.0. Experiments were performed three times and data were presented as mean ± S.D. For gel source data, see Supplementary Fig. 2.

Tango assay

Human NTSR1 (1–418) was cloned into pcDNA6 vector consisting of an expression cassette with tobacco etch virus (TEV) protease cleavage site and the transcriptional activator tTA at the C terminus. A TEV protease cDNA was fused to the C terminus of GRK2 (1–689). Interaction between NTSR1 and GRK2 leads to the cleavage of the TEV site, thus releasing tTA to trigger tTA-dependent luciferase reporter gene expression. For Tango assays, HTL cells were cultured in 24-well plate at a density of 5×10^4 cells/well for 24 h, and then transfected with 10 ng NTSR1, 10 ng GRK2 plasmids and 5 ng of phRG-tk *Renilla* luciferase expression plasmids using FuGENE HD transfection reagent. After transfection for 24 h, cells were incubated overnight with PBS (vehicle) or different concentrations of ligands. Then luciferase activities were evaluated according to manufacturer’s protocols of the Dual Luciferase Kit (Promega). Experiments were performed at least three times and data were presented as mean ± s.d.

Reporting summary

Further information on research design is available in the Nature Portfolio Reporting Summary linked to this article.

Data availability

The density maps and structure coordinates have been deposited to the Electron Microscopy Data Bank (EMDB) and the Protein Data Bank (PDB) with accession numbers EMD-36474 and 8JPB, respectively, for the NTSR1–GRK2–Gα_q complex 1; EMD-36475 and 8JPC, respectively, for the NTSR1–GRK2–Gα_q complex 2; EMD-36476 and 8JPD, respectively, for the focused refinement structure of GRK2; EMD-36477 and 8JPE, respectively, for the focused refinement structure of Gα_q; and EMD-36478 and 8JPF, respectively, for the focused refinement structure of NTSR1.

- 47. Zheng, S. Q. et al. MotionCor2: anisotropic correction of beam-induced motion for improved cryo-electron microscopy. *Nat. Methods* **14**, 331–332 (2017).
- 48. Punjani, A., Rubinstein, J. L., Fleet, D. J. & Brubaker, M. A. cryoSPARC: algorithms for rapid unsupervised cryo-EM structure determination. *Nat. Methods* **14**, 290–296 (2017).

Article

49. Punjani, A. & Fleet, D. J. 3D variability analysis: resolving continuous flexibility and discrete heterogeneity from single particle cryo-EM. *J. Struct. Biol.* **213**, 107702 (2021).
50. Pettersen, E. F. et al. UCSF Chimera—a visualization system for exploratory research and analysis. *J. Comput. Chem.* **25**, 1605–1612 (2004).
51. Emsley, P. & Cowtan, K. Coot: model-building tools for molecular graphics. *Acta Crystallogr. D* **60**, 2126–2132 (2004).
52. Croll, T. I. ISOLDE: a physically realistic environment for model building into low-resolution electron-density maps. *Acta Crystallogr. D* **74**, 519–530 (2018).
53. Adams, P. D. et al. PHENIX: a comprehensive Python-based system for macromolecular structure solution. *Acta Crystallogr. D* **66**, 213–221 (2010).
54. Pettersen, E. F. et al. UCSF ChimeraX: structure visualization for researchers, educators, and developers. *Protein Sci.* **30**, 70–82 (2020).

Acknowledgements The cryo-EM data were collected at the Advanced Center for Electron Microscopy, Shanghai Institute of Materia Medica (SIMM). The authors thank the staff at the Advanced Center for Electron Microscopy for their technical support. This work was partially supported by CAS Strategic Priority Research Program (XDB37030103 to H.E.X.); Shanghai Municipal Science and Technology Major Project (2019SHZDX02 to H.E.X.); Shanghai Municipal Science and Technology Major Project (to H.E.X.); The National Natural Science Foundation of China (32130022 to H.E.X., 82121005 to H.E.X. and D.Y., 82273961 to M.-W.W., 82273985 to D.Y. and 82204474 to F.Z.); the Lingang Laboratory (no. LG-GG-202204-01 to H.E.X.); the National Key R&D Program of China (2018YFA0507002 to H.E.X. and 2018YFA0507000 to

M.-W.W.); Young Elite Scientists Sponsorship Program by CAST (2022QNRC001 to J.D.); and Shanghai Sailing Program (23YF1456800 to J.D.).

Author contributions J.D. designed the expression constructs, purified the proteins, performed cryo-EM grid preparation and data collection, participated in functional studies and participated in figure and manuscript preparation. H.L. and Q.Y. performed cryo-EM data calculations and model building and participated in figure preparation. F.Z., Y. Ji and X. Cai performed functional studies. X.H. performed molecular dynamic simulations supervised by X. Cheng. J.L. and K.W. participated in cryo-EM data collection and calculations. X.L., W.Y., S.Z., S.L. and T.G. participated in the experiments. Y. Jiang and M.-W.W. supervised the studies. D.Y. supervised F.Z., X. Cai and S.L. for the functional studies. H.E.X. and J.D. conceived the project, analysed the structures and wrote the manuscript with input from all authors.

Competing interests The authors declare no competing interests.

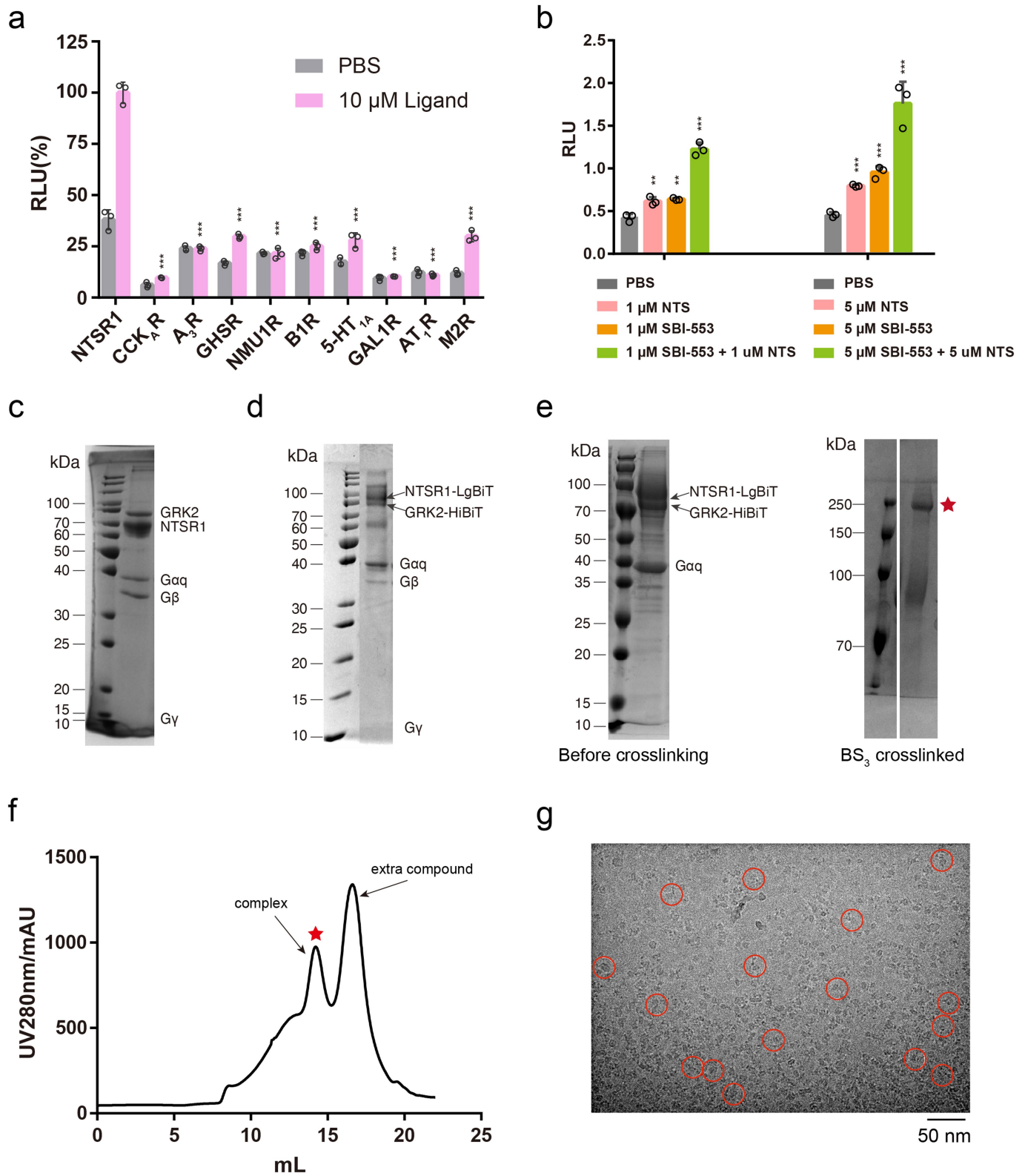
Additional information

Supplementary information The online version contains supplementary material available at <https://doi.org/10.1038/s41586-023-06395-9>.

Correspondence and requests for materials should be addressed to Jia Duan, Dehua Yang or H. Eric Xu.

Peer review information *Nature* thanks the anonymous reviewer(s) for their contribution to the peer review of this work. Peer review reports are available.

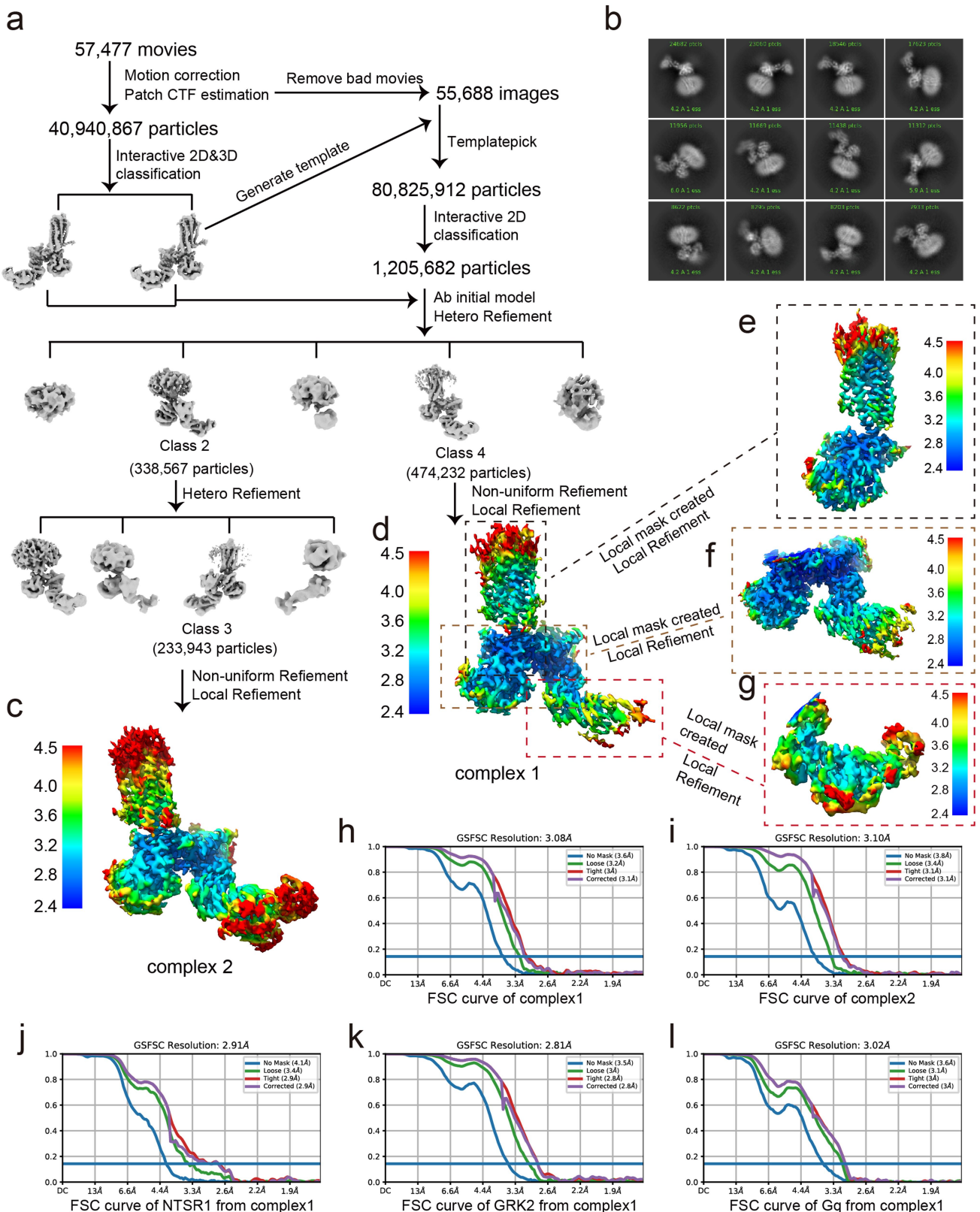
Reprints and permissions information is available at <http://www.nature.com/reprints>.



Extended Data Fig. 1 | See next page for caption.

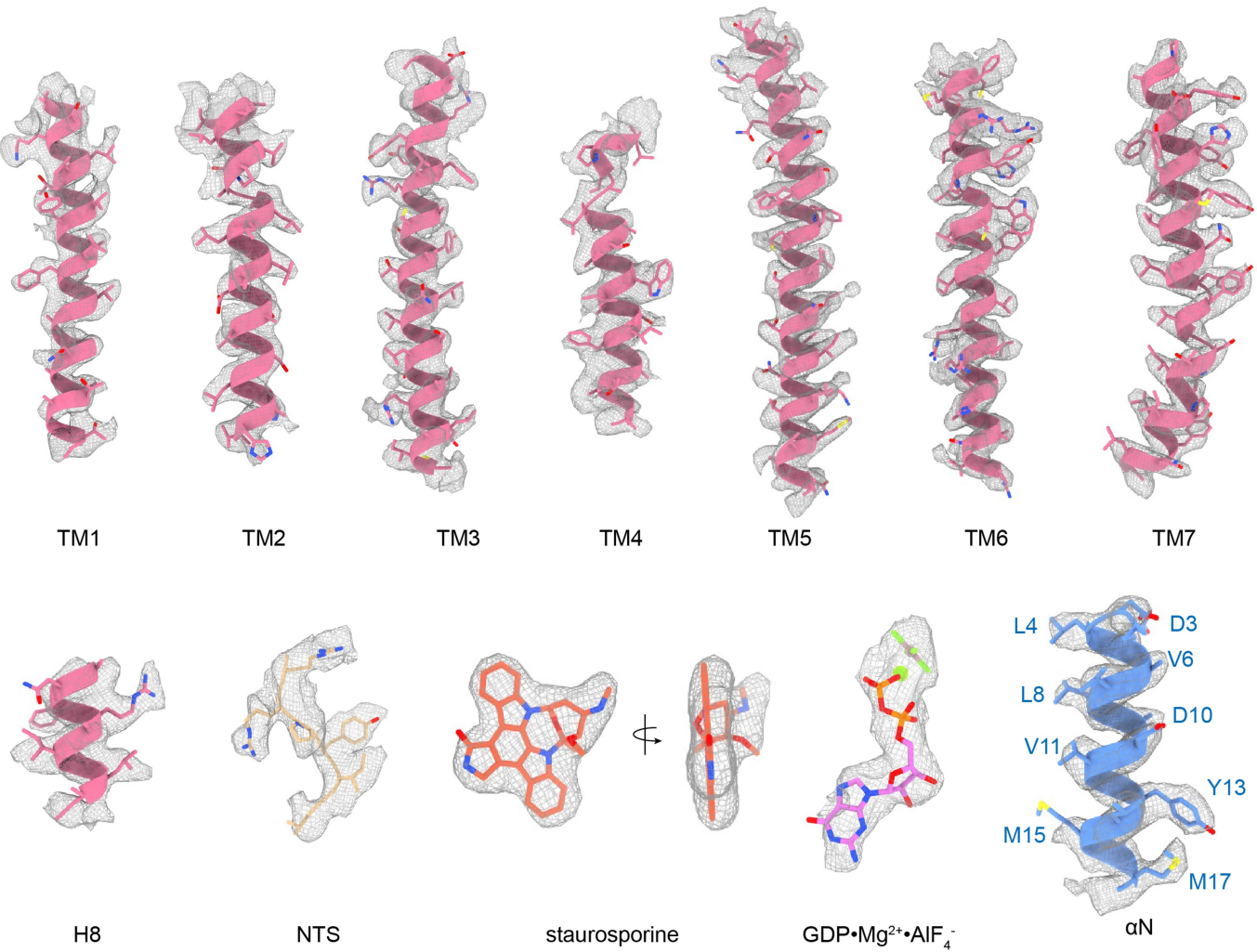
Article

Extended Data Fig. 1 | NTSR1–GRK2–G α q complex assembly. **a**, Screening for GPCR–GRK2 complexes by tango assay. RLU, relative luciferase units, which was normalized to the values of NTSR1. Data were processed as mean \pm S.D. from three independent experiments ($n = 3$), performed in triplicates. Statistical significance of differences between NTSR1 and other receptor was determined by two-sided one-way ANOVA. ** $P < 0.01$ and *** $P < 0.001$ versus NTSR1 ($P < 0.0001, <0.0001, <0.0001, <0.0001, <0.0001, <0.0001, <0.0001, <0.0001, <0.0001$ from left to right). **b**, NTS and SBI-553 improve NTSR1–GRK2 interaction determined by Tango assay. Data were processed as mean \pm S.D. from three independent experiments ($n = 3$), performed in triplicates. Statistical significance was determined by two-sided one-way ANOVA. ** $P < 0.01$ and *** $P < 0.001$ ($P = 0.0024, 0.0027, <0.0001, 0.0001, <0.0001, <0.0001$ from left to right). **c–e**, SDS-PAGE of the complexes. NTSR1–GRK2–G α q–G $\beta\gamma$ complex (**c**), NTSR1_LgBiT–GRK2_HiBiT–G α q–G $\beta\gamma$ complex (**d**), NTSR1–GRK2–G α q complex before crosslinking (left panel of **e**) and NTSR1–GRK2–G α q complex crosslinked by BS₃ (right panel of **e**). For gel source data, see Supplementary Data Fig. 1. Representative Figures from at least three independent experiments were shown. **f**, Size-exclusion chromatography elution profile of the NTSR1–GRK2–G α q complex. Red star indicates the monomer peak of the complex. **g**, Cryo-EM micrograph of the NTSR1–GRK2–G α q complex. Representative Cryo-EM micrograph from 57,477 movies was shown. Particles picked for 3D classifications were highlighted in red circles.



Extended Data Fig. 2 | Single-particle reconstruction of the NTSR1-GRK2-Gαq complex. **a**, Flowchart of cryo-EM data analysis of the NTSR1-GRK2-Gαq complex. **b**, Micrograph of the reference-free 2D class averages. **c-d**, Global Cryo-EM maps of the NTSR1-GRK2-Gαq complexes were generated and colored by local resolutions from 2.4 Å (blue) to 4.5 Å (red). **e-g**, Local Cryo-EM maps focusing on NTSR1, GRK2 bound with Gαq and only Gαq protein were generated and colored by local resolutions from 2.4 Å (blue) to 4.5 Å (red).

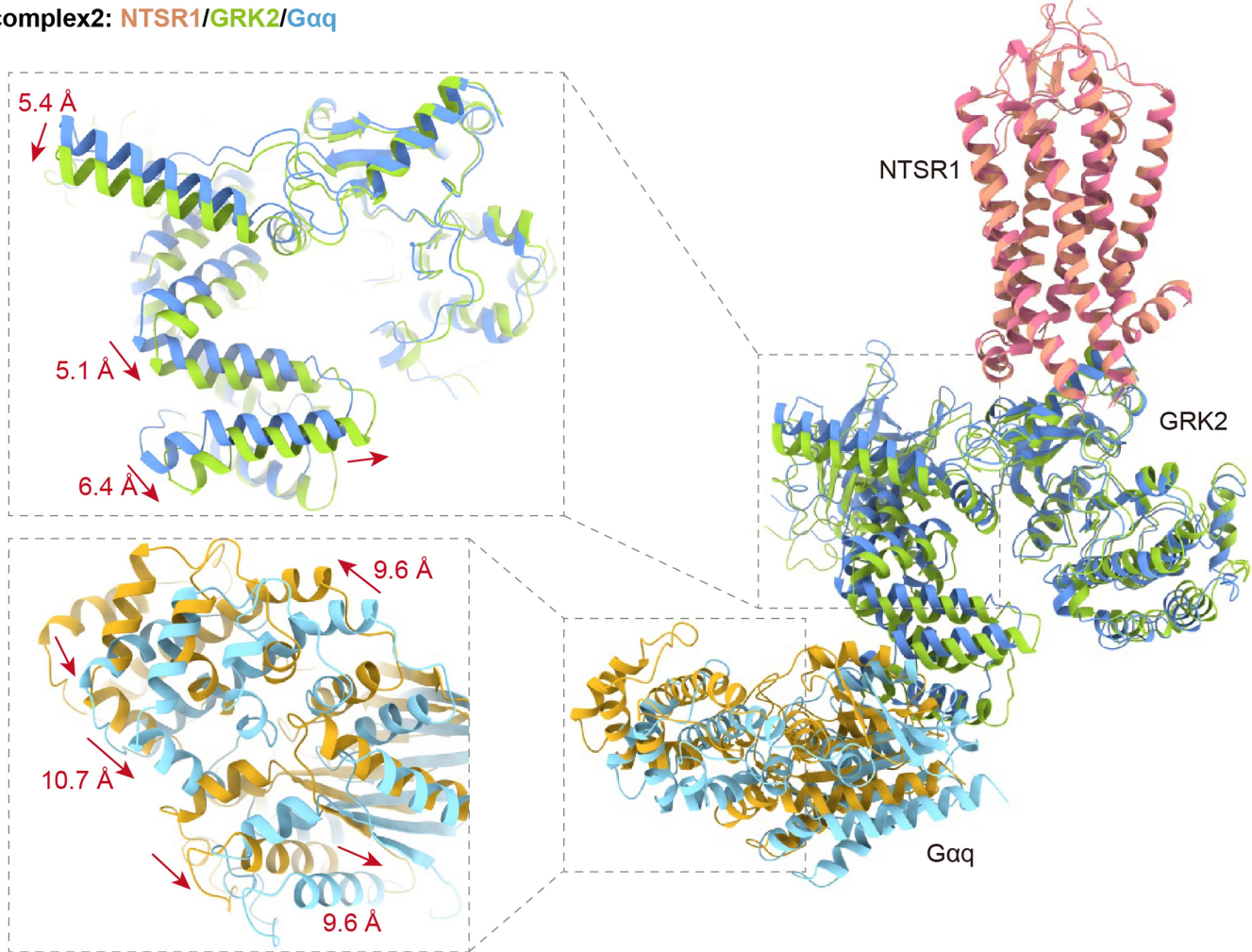
respectively. **h-l**, The “Gold-standard” Fourier shell correlation (FSC) curve indicates that the resolution of the global electron density map of the NTSR1-GRK2-Gαq complex 1 is 3.08 Å (**h**), the NTSR1-GRK2-Gαq complex 2 is 3.10 Å (**i**), and the resolution of the local electron density maps of NTSR1 (contains a partial of GRK2), GRK2 bound with Gαq and only Gαq protein from complex 1 are 2.91 Å (**j**), 2.81 Å (**k**) and 3.02 Å (**l**), respectively.



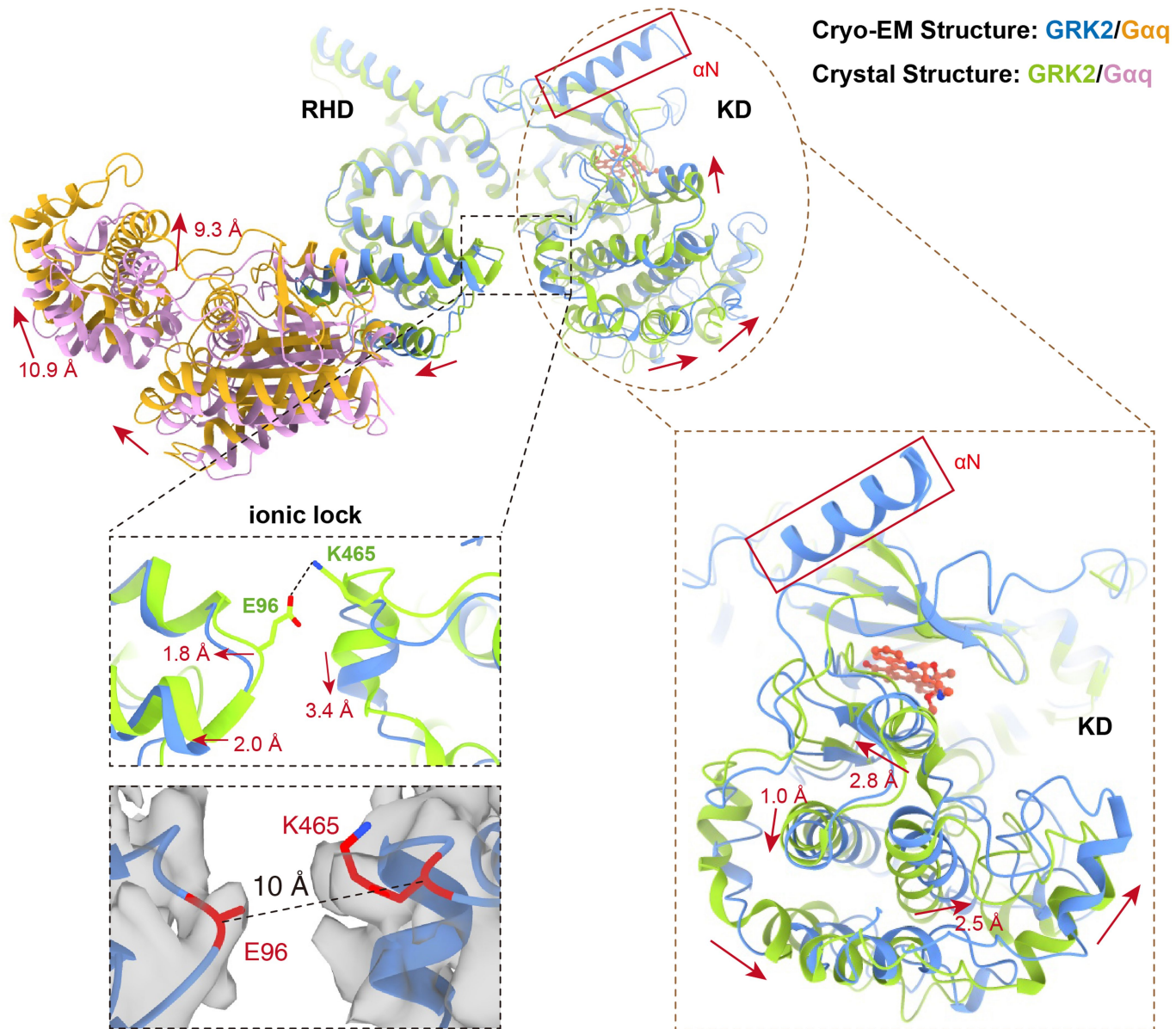
Extended Data Fig. 3 | Cryo-EM density maps with all transmembrane helices, and H8 of NTSR1, NTS, staurosporine, GDP•Mg²⁺•AlF₄⁻ and αN of GRK2. The density map is shown at contour levels of 0.36, 0.34, 0.29, 0.30, 0.30, 0.29, 0.41, 0.32, 0.22, 0.83, 0.28 and 0.43, respectively, with carve radii of 2.0 Å.

complex1: NTSR1/GRK2/G_qq

complex2: NTSR1/GRK2/G_qq

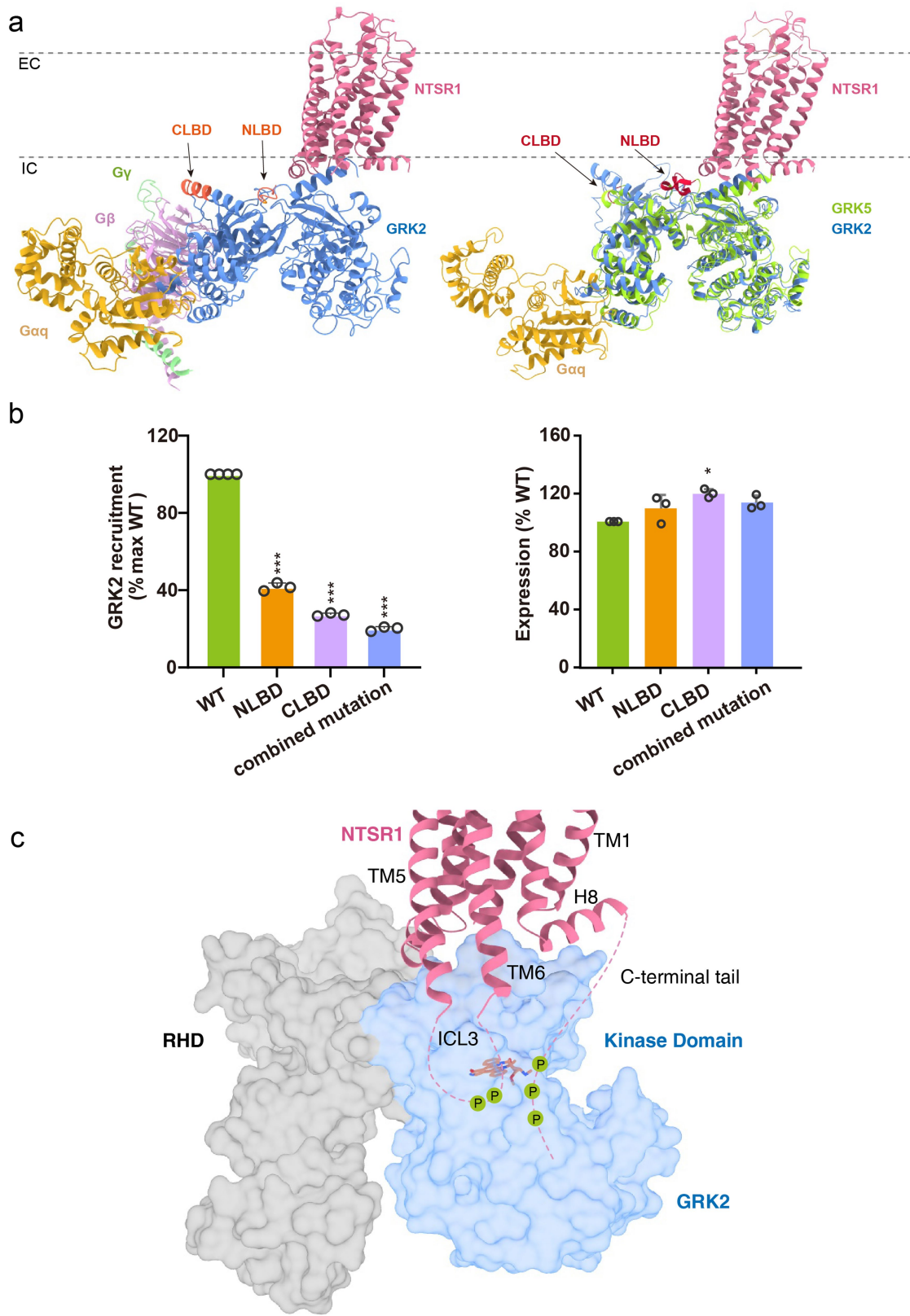


Extended Data Fig. 4 | Structural comparison of the NTSR1–GRK2–G_qq complex 1 and 2. Comparison of these two complexes reveals that they have very similar NTSR1 structure but a swing of GRK2 and G_qq of ~5–10 Å related to NTSR1. The red arrows are referring to the movement between two structures.



Extended Data Fig. 5 | Structural comparison of the GRK2-Gαq from the cryo-EM structure NTSR1-GRK2-Gαq complex with the crystal structure of GRK2-Gαq-Gβγ. Comparing the GRK2 structure from the NTSR1 complex to the crystal structure of GRK2 from the complex with Gαq and Gβγ reveals three major differences. The GRK2 structure from the NTSR1 complex contains a

N-terminal helix that is packed onto the kinase domain, has a breakage in the ionic lock between its RHD from the KD, and adopts a closed conformation in its KD by 2-3 Å shifts of the KD relative to the KD of GRK2 from the crystal structure. The density map is shown at a level of 0.28. The red arrows are referring to the movement between two structures.



Extended Data Fig. 6 | See next page for caption.

Article

Extended Data Fig. 6 | Possible Lipid binding sites and phosphorylation sites. **a**, G $\beta\gamma$ subunits was modeled into the NTSR1–GRK2 structure by structural alignment of GRK2 from NTSR1–GRK2 structure and GRK2–G α q–G $\beta\gamma$ structure complex (PDB code: 2BCJ). GRK2 was shown in blue and GRK5 (PDB code: 6PJX) was shown in green. The possible lipid binding sites from GRK2 are highlighted in orange and GRK5 are highlighted in dark red. NLBD, the N-terminal lipid binding site. CLBD, the C-terminal lipid binding site. **b**, WT and mutated GRK2 recruitment to NTSR1 induced by NTS (left panel), relative expression level of WT and mutated GRK2 (right panel). NLBD refers to the combined mutations of N-terminal basic residues (R27A, K30A, K31A). CLBD

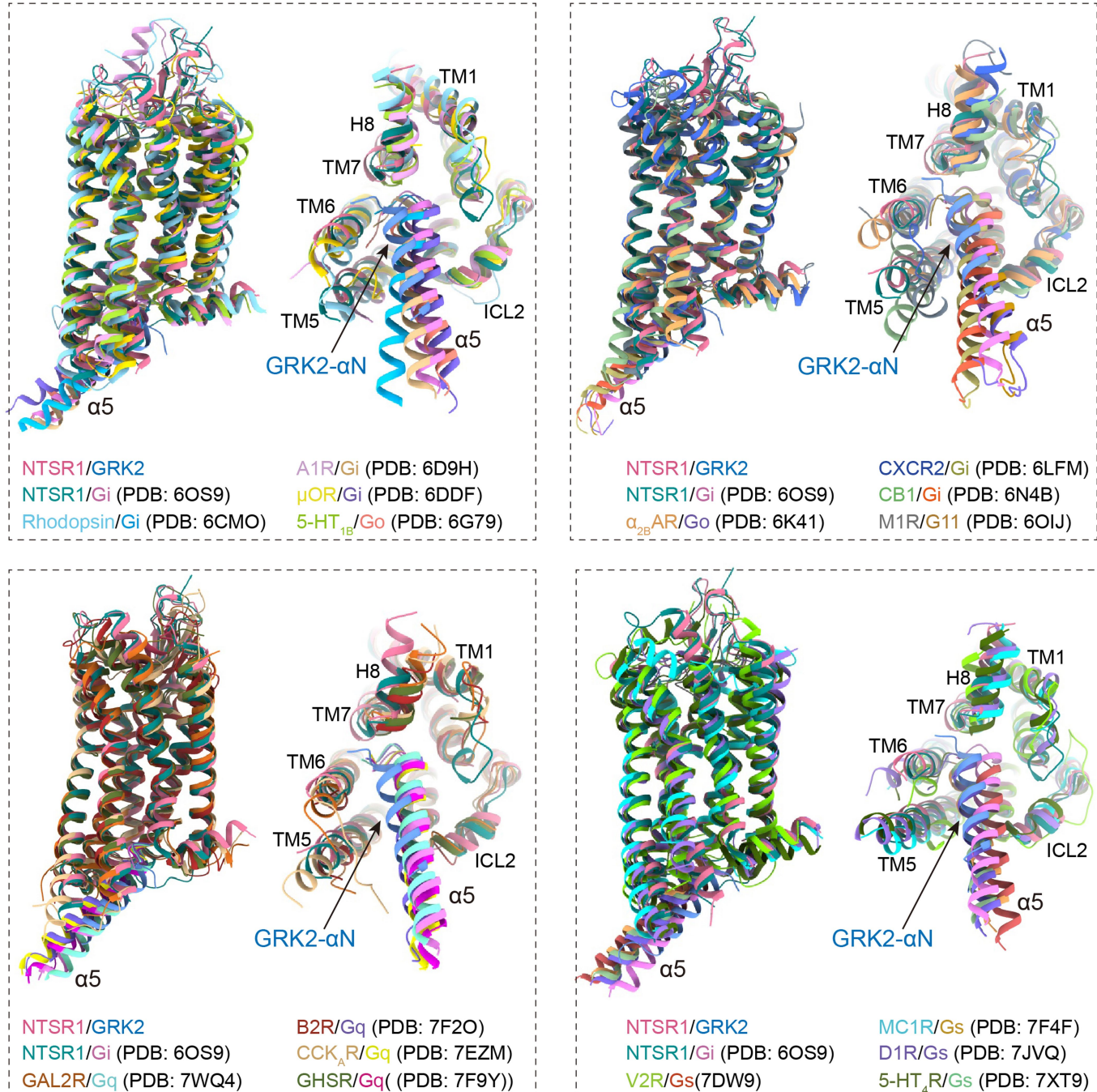
means the combined mutations R535A, R539A, K540A, K541A, K543A, K545A. Combined mutation refers to all the mutations combined. Data were shown as mean \pm S.D. from three independent experiments ($n = 3$), performed in duplicate. Statistical significance of differences between WT and mutants was determined by two-sided one-way ANOVA. * $P < 0.05$ and ** $P < 0.01$ and *** $P < 0.001$ versus WT. The detailed information is provided in Extended Data Table 3. **c**, Phosphorylation sites of the active NTSR1. The extended loop of ICL3 or the elongated C-terminal tail of NTSR1 could reach the active cleft of GRK2, thus are available to be phosphorylated by GRK2. P represents phosphorylation modifications.



Extended Data Fig. 7 | Sequence alignment of human GRKs. The N-terminal helix (α N) is highlighted in red. The RHD is highlighted in green and KD is in light blue. The AST loop extended from the kinase domain is in light purple. The PHD of GRK2 and GRK3 are in pink. N-terminal lipid binding domain (NLBD) and

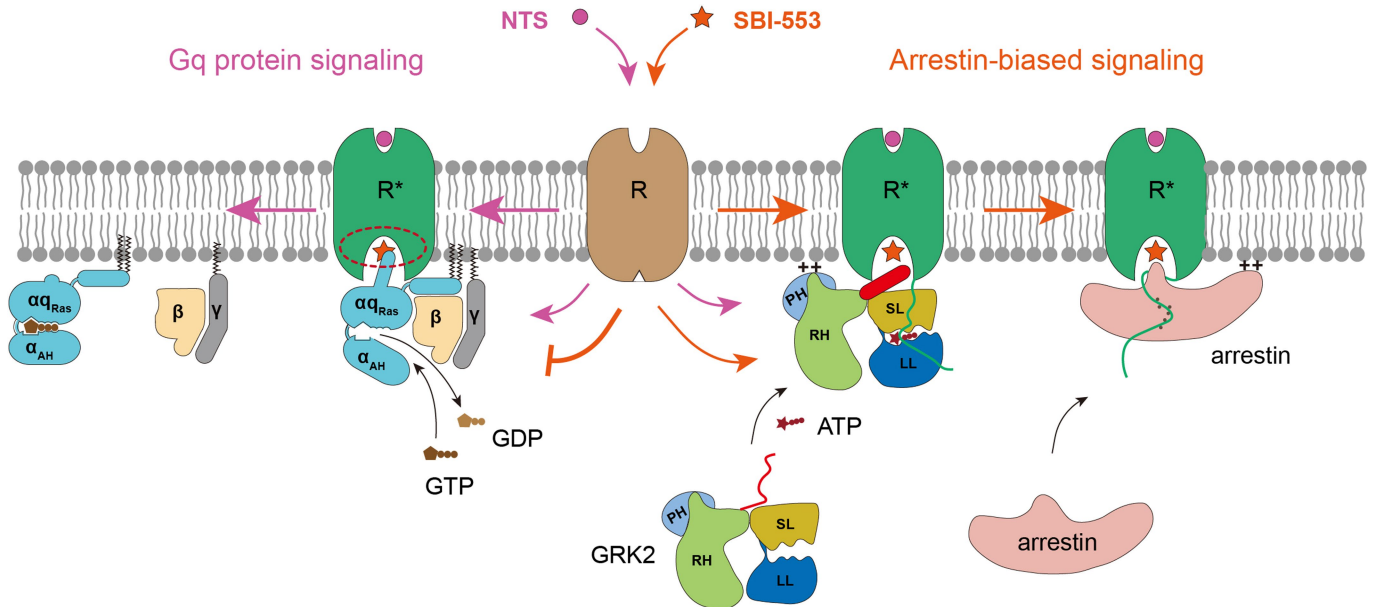
C-terminal lipid binding domain (NLBD) according to GRK5 are highlighted in dark yellow and light green, respectively. Residues that may interact with membrane lipid are highlighted in dark blue. And residues from GRK2 that interact with NTSR1 are highlighted in yellow. α , α helix, β , β strand.

Article



Extended Data Fig. 8 | Structural comparison of NTSR1–GRK2–Gαq complex with NTSR–Gi complex and other GPCR–G protein complexes.
Superposition of the receptor TMD fragment from different GPCR complexes

showed that the active GPCRs had very similar 3D architecture, and the location of α5 helix from different G proteins overlapped with the N-terminal helix of GRK2.



Extended Data Fig. 9 | Gq protein and arrestin signaling of NTSR1 potentiated by NTS and SBI-553. NTS is a balanced agonist, which binds to orthosteric site and promotes NTSR1 to mediate both G protein and arrestin signaling. SBI-553 is an arrestin-biased allosteric modulator, which binds to the

intracellular site and promotes GRK2 binding and arrestin signaling, but blocks Gq protein binding and signaling (red circled star). ++ marks indicate membrane binding.

Article

Extended Data Table 1 | Cryo-EM data collection, refinement and validation statistics

	NTSR1-GRK2-Gαq complex1 (EMDB-36474) (PDB 8JPB)	NTSR1-GRK2-Gαq complex2 (EMDB-36475) (PDB 8JPC)
Data collection and processing		
Magnification	105,000	
Voltage (kV)	300	
Electron exposure (e-/Å ²)	50	
Defocus range (μm)	-1.2 to -2.2	
Pixel size (Å)	0.824	
Symmetry imposed	C1	
Initial particle images (no.)	80,825,912	
Final particle images (no.)	474,232	233,943
Map resolution (Å)	3.08	3.10
FSC threshold	0.143	0.143
Map resolution range (Å)	2.4 - 4.5	2.4 - 4.5
Refinement		
Initial model used (PDB code)	2BCJ, 4RGV, AlphaFold-NTSR1	2BCJ, 4RGV, AlphaFold-NTSR1
Map sharpening <i>B</i> factor (Å ²)	-129.5	-116.6
Model composition		
Non-hydrogen atoms	9655	9501
Protein residues	1279	1277
Ligands	4	4
Nucleotide	1	1
<i>B</i> factors (Å ²)		
Protein	66.42	70.94
Ligand	103.05	63.37
Nucleotide	55.66	44.99
R.m.s. deviations		
Bond lengths (Å)	0.005	0.004
Bond angles (°)	1.009	0.888
Validation		
MolProbity score	1.67	1.73
Clashscore	4.82	4.51
Poor rotamers (%)	0.00	0.00
Ramachandran plot		
Favored (%)	96.45	96.44
Allowed (%)	3.55	3.56
Disallowed (%)	0.00	0.00

Extended Data Table 2 | NTS and SBI-553 induced GRK2, β-arrestin-2 and Gq recruitment to NTSR1

Ligand	Constructs	pEC ₅₀	p value (for pEC ₅₀)	E _{min}	p value (for E _{min})	E _{max}	p value (for E _{max})	Sample size (n value)
NTS	NTSR1 (WT) - GRK2 (WT)	9.02 ± 0.05	-	~ 0	-	100 ± 1.78	-	3
	NTSR1 (WT) - β-arrestin2 (3A)	9.05 ± 0.02	-	~ 0	-	100 ± 0.58	-	3
	NTSR1 (WT) - Gq	8.25 ± 0.07	-	~ 0	-	100 ± 2.52	-	3
SBI-553	NTSR1 (WT) - GRK2 (WT)	5.31 ± 0.17***	<0.0001	-1.66 ± 1.93	0.2111	39.64 ± 3.61***	<0.0001	3
	NTSR1 (WT) - β-arrestin2 (3A)	5.01 ± 0.08***	<0.0001	0.36 ± 0.11**	0.0053	6.44 ± 0.29***	<0.0001	3
	NTSR1 (WT) - Gq	UD	-	UD	-	UD	-	3
NTS + 0 μM SBI-553	NTSR1 (WT) - GRK2 (WT)	9.02 ± 0.05	-	~ 0	-	100 ± 1.77	-	3
	NTSR1 (WT) - β-arrestin2 (3A)	9.05 ± 0.02	-	~ 0	-	100 ± 0.59	-	3
NTS + 1 μM SBI-553	NTSR1 (WT) - GRK2 (WT)	8.82 ± 0.12	0.0832	14.44 ± 2.94***	0.0005	107.80 ± 3.69*	0.0366	3
	NTSR1 (WT) - β-arrestin2 (3A)	9.17 ± 0.04*	0.0162	1.05 ± 1.10	0.4994	101.96 ± 1.24	0.2169	3
NTS + 5 μM SBI-553	NTSR1 (WT) - GRK2 (WT)	8.89 ± 0.11	0.2637	26.45 ± 2.77***	<0.0001	117.45 ± 3.40***	0.0008	3
	NTSR1 (WT) - β-arrestin2 (3A)	9.26 ± 0.06**	0.0011	2.16 ± 1.78	0.1208	116.39 ± 1.95***	<0.0001	3

Data represent mean pEC₅₀ (pEC₅₀ ± S.D.), E_{max} (E_{max} ± S.D.), E_{min} (E_{min} ± S.D.). Data were generated and graphed as means ± S.D. of at least three independent experiments (n=3) performed in duplicate. The E_{min} and E_{max} were normalized by NTS-induced WT receptor within each individual experiment, with the basal activity as zero, while the fitted E_{max} as 100. UD, undetectable.

Article

Extended Data Table 3 | Ligands-induced GRK2 recruitment to NTSR1

Ligand	Constructs	Span (% WT)	p value (for Span)	Sample size (n value)	Expression (% WT)	p value (for expression)	Sample size (n value)
NTS	NTSR1 (WT)	100	-	4	100	-	4
	NTSR1 (F174G)	45.99 ± 4.99***	<0.0001	4	66.65 ± 5.37**	0.0090	3
	NTSR1 (K177G)	72.51 ± 20.54*	0.0248	4	66.09 ± 4.49**	0.0080	3
	NTSR1 (T178G)	87.66 ± 7.09	0.5803	3	67.63 ± 16.77**	0.0064	4
	NTSR1 (PF)	45.73 ± 12.51***	<0.0001	4	79.37 ± 16.81	0.1321	3
	NTSR1 (PFKT)	48.07 ± 15.41***	<0.0001	4	89.20 ± 13.83	0.6515	3
	GRK2 (WT)	100	-	3	100	-	3
	GRK2 (D3G)	38.99 ± 2.88***	<0.0001	3	114.61 ± 6.74	0.1288	3
	GRK2 (L4G)	33.89 ± 3.37***	<0.0001	3	122.87 ± 21.16*	0.0214	3
	GRK2 (V7G)	28.82 ± 3.85***	<0.0001	3	121.04 ± 12.84*	0.0328	3
	GRK2 (L8G)	39.01 ± 2.81***	<0.0001	3	136.64 ± 18.42***	0.0006	3
	GRK2 (V11G)	35.30 ± 4.80***	<0.0001	3	97.23 ± 9.26	0.7680	3
	GRK2 (M15G)	31.58 ± 1.75***	<0.0001	3	118.92 ± 2.67	0.0527	3
	GRK2 (V7L8)	28.38 ± 3.59***	<0.0001	3	105.22 ± 15.77	0.5789	3
	GRK2 (L4V7L8)	25.50 ± 1.34***	<0.0001	3	116.26 ± 9.60	0.0926	3
	GRK2 (WT)	100	-	3	100	-	3
	GRK2 (NLBD)	41.65 ± 2.10***	<0.0001	3	113.10 ± 4.93	0.1711	3
	GRK2 (CLBD)	27.36 ± 0.80***	<0.0001	3	119.50 ± 2.96*	0.0464	3
	GRK2 (Combined mutation)	20.03 ± 1.13***	<0.0001	3	109.07 ± 9.40	0.3385	3
SBI-553	NTSR1 (WT)	100	-	7	100	-	6
	NTSR1 (L162F)	60.74 ± 12.71***	<0.0001	5	81.97 ± 11.33	0.0537	4
	NTSR1 (L162W)	56.81 ± 18.73***	<0.0001	4	64.17 ± 17.69***	0.0003	3
	NTSR1 (L305W)	40.63 ± 16.50***	<0.0001	4	94.24 ± 5.99	0.9333	3
	NTSR1 (L305Y)	46.44 ± 7.82***	<0.0001	4	58.71 ± 12.11***	<0.0001	5
	NTSR1 (V367F)	42.91 ± 7.10***	<0.0001	4	63.61 ± 9.58***	<0.0001	5
	NTSR1 (V367Y)	43.74 ± 8.91***	<0.0001	5	65.36 ± 9.99***	0.0001	4

Data represent mean Span (Span ± S.D.). Span is equal to the high concentration response minus the low concentration response. The high and low concentration of NTS are 1 μM and 0 μM. The high and low concentration of SBI-553 are 25 μM and 0 μM. Data were generated and graphed as means ± S.D. of at least three independent experiments ($n \geq 3$) performed in duplicate. Statistical significance of differences between WT and mutants was determined by two-sided one-way ANOVA. * $P < 0.05$, ** $P < 0.01$ and *** $P < 0.001$ versus WT.

Reporting Summary

Nature Portfolio wishes to improve the reproducibility of the work that we publish. This form provides structure for consistency and transparency in reporting. For further information on Nature Portfolio policies, see our [Editorial Policies](#) and the [Editorial Policy Checklist](#).

Statistics

For all statistical analyses, confirm that the following items are present in the figure legend, table legend, main text, or Methods section.

n/a Confirmed

- The exact sample size (n) for each experimental group/condition, given as a discrete number and unit of measurement
- A statement on whether measurements were taken from distinct samples or whether the same sample was measured repeatedly
- The statistical test(s) used AND whether they are one- or two-sided
Only common tests should be described solely by name; describe more complex techniques in the Methods section.
- A description of all covariates tested
- A description of any assumptions or corrections, such as tests of normality and adjustment for multiple comparisons
- A full description of the statistical parameters including central tendency (e.g. means) or other basic estimates (e.g. regression coefficient) AND variation (e.g. standard deviation) or associated estimates of uncertainty (e.g. confidence intervals)
- For null hypothesis testing, the test statistic (e.g. F , t , r) with confidence intervals, effect sizes, degrees of freedom and P value noted
Give P values as exact values whenever suitable.
- For Bayesian analysis, information on the choice of priors and Markov chain Monte Carlo settings
- For hierarchical and complex designs, identification of the appropriate level for tests and full reporting of outcomes
- Estimates of effect sizes (e.g. Cohen's d , Pearson's r), indicating how they were calculated

Our web collection on [statistics for biologists](#) contains articles on many of the points above.

Software and code

Policy information about [availability of computer code](#)

Data collection Cyro-EM data were automatically collected using EPU 2.12 on a Titan Krios.

Data analysis The following softwares were used in this study: MotionCor 2.1, CryoSPARC-v3.3.1, UCSF Chimera 1.14, UCSF ChimeraX 1.3, Phenix 1.18, Coot 0.9.4.1, ISOLDE 1.2, Pymol 2.0.3.0., ImageJ, BD Accuri C6 software 1.0.264.21., GraphPad Prism 9.0.

For manuscripts utilizing custom algorithms or software that are central to the research but not yet described in published literature, software must be made available to editors and reviewers. We strongly encourage code deposition in a community repository (e.g. GitHub). See the Nature Portfolio [guidelines for submitting code & software](#) for further information.

Data

Policy information about [availability of data](#)

All manuscripts must include a [data availability statement](#). This statement should provide the following information, where applicable:

- Accession codes, unique identifiers, or web links for publicly available datasets
- A description of any restrictions on data availability
- For clinical datasets or third party data, please ensure that the statement adheres to our [policy](#)

The density maps and structure coordinates have been deposited to the Electron Microscopy Database (EMDB) and the Protein Data Bank (PDB) with accession number of EMD-36474, PDB ID 8JPB for the NTSR1-GRK2-Gαq complex 1; EMD-36475 and 8JPC for the NTSR1-GRK2-Gαq complex 2; EMD-36476 and 8JPD for the

focused refinement structure of GRK2; EMD-36477 and 8JPE for the focused refinement structure of Gαq; EMD-36478 and 8JPF for the focused refinement structure of NTSR1.

Human research participants

Policy information about [studies involving human research participants and Sex and Gender in Research](#).

Reporting on sex and gender

Use the terms sex (biological attribute) and gender (shaped by social and cultural circumstances) carefully in order to avoid confusing both terms. Indicate if findings apply to only one sex or gender; describe whether sex and gender were considered in study design whether sex and/or gender was determined based on self-reporting or assigned and methods used. Provide in the source data disaggregated sex and gender data where this information has been collected, and consent has been obtained for sharing of individual-level data; provide overall numbers in this Reporting Summary. Please state if this information has not been collected. Report sex- and gender-based analyses where performed, justify reasons for lack of sex- and gender-based analysis.

Population characteristics

Describe the covariate-relevant population characteristics of the human research participants (e.g. age, genotypic information, past and current diagnosis and treatment categories). If you filled out the behavioural & social sciences study design questions and have nothing to add here, write "See above."

Recruitment

Describe how participants were recruited. Outline any potential self-selection bias or other biases that may be present and how these are likely to impact results.

Ethics oversight

Identify the organization(s) that approved the study protocol.

Note that full information on the approval of the study protocol must also be provided in the manuscript.

Field-specific reporting

Please select the one below that is the best fit for your research. If you are not sure, read the appropriate sections before making your selection.

Life sciences Behavioural & social sciences Ecological, evolutionary & environmental sciences

For a reference copy of the document with all sections, see nature.com/documents/nr-reporting-summary-flat.pdf

Life sciences study design

All studies must disclose on these points even when the disclosure is negative.

Sample size

For cryo-EM data, images were collected until the resolution and 3D reconstruction converges. 57,477 movies of NTSR1-GRK2-Gαq complex were collected using a Titan Krios equipped with a Gatan K3 Summit direct electron detector. For all the functional assay, no statistical approaches were used to predetermine the sample size. We use sample size at least of three independent experiments, commonly exploited by researchers in this field.

Data exclusions

No data were systematically excluded from the analysis except badly picked or low resolution particles from cryo-EM data.

Replication

Each experiment was reproduced at least three times independently. Experimental findings were reliably reproduced.

Randomization

No Randomization was attempted or needed. Randomization was not necessary as the independent variables to be tested were sufficient for the functional interpretation within this study.

Blinding

Blinding is not necessary or valid for the purposes of structural determination. For cryo-EM study, purified NTSR1-GRK2-Gαq complex were applied onto a glow-discharged holey carbon grid and subsequently vitrified using a Vitrobot Mark IV. Cryo-EM data were then collected automatically. For functional analysis, blinding was not necessary due to the quantitative nature of the experiment. All experimental data acquired or analyzed in this study are included in this published article, and subjected to statistical analysis whenever necessary.

Reporting for specific materials, systems and methods

We require information from authors about some types of materials, experimental systems and methods used in many studies. Here, indicate whether each material, system or method listed is relevant to your study. If you are not sure if a list item applies to your research, read the appropriate section before selecting a response.

Materials & experimental systems

n/a	Involved in the study
<input type="checkbox"/>	<input checked="" type="checkbox"/> Antibodies
<input type="checkbox"/>	<input checked="" type="checkbox"/> Eukaryotic cell lines
<input checked="" type="checkbox"/>	<input type="checkbox"/> Palaeontology and archaeology
<input checked="" type="checkbox"/>	<input type="checkbox"/> Animals and other organisms
<input checked="" type="checkbox"/>	<input type="checkbox"/> Clinical data
<input checked="" type="checkbox"/>	<input type="checkbox"/> Dual use research of concern

Methods

n/a	Involved in the study
<input checked="" type="checkbox"/>	<input type="checkbox"/> ChIP-seq
<input type="checkbox"/>	<input checked="" type="checkbox"/> Flow cytometry
<input checked="" type="checkbox"/>	<input type="checkbox"/> MRI-based neuroimaging

Antibodies

Antibodies used

For measurement of receptor cell surface expression, monoclonal anti-FLAG M2 antibody (Sigma Aldrich, NO.F3165) and donkey anti-mouse IgG(H+L) Highly Cross-Adsorbed Secondary Antibody, Alexa Fluor 488 (Invitrogen, NO.A-21202) were used. The primary antibody was used in 1:300 dilution, and the secondary antibody in 1:1000 dilution.

For measurement of GRK2 expression, mouse anti-FLAG antibody (Abclonal, NO.AE005), rabbit β-tubulin antibody (Abclonal, NO.A12289), HRP-conjugated Goat Anti-Mouse IgG (H+L) (Abclonal, AS003) and anti-rabbit IgG (H+L) antibodies (Abclonal, AS014) were used. The primary mouse anti-FLAG antibody was used in 1:1000 dilution, β-tubulin antibody was used in 1:5000 dilution and the secondary antibodies were used in 1:10000 dilution.

Validation

Monoclonal ANTI-FLAG® M2 antibody: <https://www.sigmaldrich.com/catalog/product/sigma/f3165?lang=en®ion=US>
 Donkey anti-Mouse IgG (H+L) Highly Cross-Adsorbed Secondary Antibody, Alexa Fluor 488: <https://www.thermofisher.cn/cn/zh/antibody/product/Donkey-anti-Mouse-IgG-H-L-Highly-Cross-Adsorbed-Secondary-Antibody-Polyclonal/A-21202>
 mouse anti-FLAG antibody: <https://abclonal.com.cn/catalog/AE005>, HRP-conjugated Goat Anti-Mouse IgG (H+L) antibody: <https://abclonal.com.cn/catalog/AS003>, rabbit β-tubulin antibody: <https://abclonal.com.cn/catalog/A12289>, HRP-conjugated Goat Anti-rabbit IgG (H+L) antibody: <https://abclonal.com.cn/catalog/AS014>.

All antibodies used are commercially purchased and have been validated by the vendors. Validation data are available from the respective vendor's respective websites.

Eukaryotic cell lines

Policy information about [cell lines and Sex and Gender in Research](#)

Cell line source(s)

Hi5 insect cells (Invitrogen); HEK293T cells (ATCC); HTL cells (a gift from G. Barnea and R. Axel (Brown University and Columbia University))

Authentication

All of the cell lines are maintained by the supplier. No additional authentication was performed by the authors of this study.

Mycoplasma contamination

The above cell lines were negative for Mycoplasma contamination.

Commonly misidentified lines (See [ICLAC](#) register)

No commonly misidentified cell lines were used.

Flow Cytometry

Plots

Confirm that:

- The axis labels state the marker and fluorochrome used (e.g. CD4-FITC).
- The axis scales are clearly visible. Include numbers along axes only for bottom left plot of group (a 'group' is an analysis of identical markers).
- All plots are contour plots with outliers or pseudocolor plots.
- A numerical value for number of cells or percentage (with statistics) is provided.

Methodology

Sample preparation

HEK293T cells were grown for 24 h to reach 70% to 80% confluence (6-well plate), then the cells were transiently transfected with 4 ug WT or mutated NTSR1 every hole. After 24 h of transfection, cells were washed once with PBS and then detached with 0.2% (w/v) EDTA in PBS. Cells were blocked with PBS containing 5% (w/v) BSA for 15 min at room temperature before incubating with primary anti-Flag M2 antibody (diluted with PBS containing 5% BSA at a ratio of 1:300, Sigma-Aldrich) for 1 h at room temperature. Cells were then washed three times with PBS containing 1% (w/v) BSA and then incubated with anti-mouse Alexa-488-conjugated secondary antibody (diluted at a ratio of 1:1,000, Invitrogen) at 4 °C in the dark for 1 h. After another three times of washing, cells were collected, and fluorescence intensity was quantified in a BD Accuri C6 flow cytometer system (BD Biosciences) through a BD Accuri C6 software 1.0.264.21 at excitation 488 nm and emission 519 nm. Approximately 10,000 cellular events per sample were collected.

Instrument

BD Accuri C6 (BD Biosciences)

Software

BD Accuri C6 software (version 1.0.264.21)

Cell population abundance

Approximately 10,000 cellular events were collected and the total fluorescence intensity of positive expression cell population was calculated.

Gating strategy

Gating was determined by the Alexa-488 fluorescence intensity to differentiate positive cells and all other cells.

Tick this box to confirm that a figure exemplifying the gating strategy is provided in the Supplementary Information.